JGR Planets

RESEARCH ARTICLE

Key Points:

- Clast-poor impact breccias on Endeavour crater rim are distal ejecta from at least two earlier impacts
- Enrichments in Si and Al, and smectite formation are unique to pre-Endeavour rocks; post-Endeavour alteration formed Ca- and Mg-sulfates
- Magnesium, Ca and Cl have been mobilized by transient thin films of water acting on salts very recently, and could be ongoing

Correspondence to:

D. W. Mittlefehldt,
david.w.mittlefehldt@nasa.gov

Author Contributions:

Conceptualization: David W. Mittlefehldt
Formal analysis: Ralf Gellert, Scott vanBommel
Methodology: Ralf Gellert, Scott vanBommel
Project Administration: Raymond E. Arvidson
Validation: Ralf Gellert, Scott vanBommel
Writing – original draft: David W. Mittlefehldt

Geology and Geochemistry of Noachian Bedrock and Alteration Events, Meridiani Planum, Mars: MER Opportunity Observations

David W. Mittlefehldt[1] , **Ralf Gellert[2]** , **Scott vanBommel[2,3]** , **Raymond E. Arvidson[3]**, **James W. Ashley[4]**, **Benton C. Clark[5]** , **Larry S. Crumpler[6]** , **William H. Farrand[5]** , **Matthew P. Golombek[4]**, **John A. Grant[7]** , **Richard V. Morris[1]** , and **Christian Schröder[8]**

[1]Astromaterials Research Office, NASA/Johnson Space Center, Houston, TX, USA, [2]Department of Physics, University of Guelph, Guelph, ON, Canada, [3]Department of Earth and Planetary Sciences, Washington University in Saint Louis, Saint Louis, MO, USA, [4]Jet Propulsion Laboratory, California Institute of Technology, Pasadena, CA, USA, [5]Space Science Institute, Boulder, CO, USA, [6]New Mexico Museum of Natural History and Science, Albuquerque, NM, USA, [7]Smithsonian Institution, NASM CEPS, Washington, DC, USA, [8]Biological and Environmental Sciences, University of Stirling, Scotland, UK

Abstract We have used Mars Exploration Rover Opportunity data to investigate the origin and alteration of lithic types along the western rim of Noachian-aged Endeavour crater on Meridiani Planum. Two geologic units are identified along the rim: the Shoemaker and Matijevic formations. The Shoemaker formation consists of two types of polymict impact breccia: clast-rich with coarser clasts in upper units; clast-poor with smaller clasts in lower units. Comparisons with terrestrial craters show that the lower units represent more distal ejecta from at least two earlier impacts, and the upper units are proximal ejecta from Endeavour crater. Both are mixtures of target rocks of basaltic composition with subtle compositional variations caused by differences in post-impact alteration. The Matijevic formation and lower Shoemaker units represent pre-Endeavour geology, which we equate with the regional Noachian subdued cratered unit. An alteration style unique to these rocks is formation of smectite and Si- and Al-rich vein-like structures crosscutting outcrops. Post-Endeavour alteration is dominated by sulfate formation. Rim-crossing fracture zones include regions of alteration that produced Mg-sulfates as a dominant phase, plausibly closely associated in time with the Endeavour impact. Calcium-sulfate vein formation occurred over extended time, including before the Endeavour impact and after the Endeavour rim had been substantially degraded, likely after deposition of the Burns formation that surrounds and embays the rim. Differences in Mg, Ca and Cl concentrations on rock surfaces and interiors indicate that mobilization of salts by transient water has occurred recently and may be ongoing.

Plain Language Summary Data returned by the Mars Exploration Rover Opportunity was used to investigate rock origins along the western rim of Endeavour crater on Meridiani Planum, Mars. The Shoemaker formation consists of impact-formed breccia of two types: coarser-grained upper subunits and finer-grained lower subunits. The lower units represent ejecta from at least two older, more distant craters, while the upper units are ejecta from Endeavour crater. Subtle compositional differences are caused by differences in post-impact alteration along the crater rim. The lower Shoemaker units represent part of the pre-Endeavour rock sequence. An alteration style unique to these rocks is formation of Si- and Al-rich structures crosscutting bedrock. Post-Endeavour alteration is dominated by sulfate formation. Fracture zones in the rim include regions of alteration that produced Mg-sulfates as a dominant phase, plausibly closely associated in time with the Endeavour impact. Calcium-sulfate vein formation occurred over extended time, some before the Endeavour impact and some much later, likely after deposition of the sulfate-rich sandstones of Meridiani Planum. Differences in composition of rock surfaces and interiors indicate that mobilization of salts by transient water has occurred recently and may be ongoing on Mars.

1. Introduction

Mars Exploration Rover (MER) Opportunity explored the geology of Meridiani Planum within Arabia Terra for 5111 Sols (Mars days), from landing (January 25, 2004) through the loss of signal (June 19, 2018) caused by a global dust storm that choked off her solar energy supply. During the first seven and a half Earth years

Writing – review & editing: David W. Mittlefehldt, Ralf Gellert, Raymond E. Arvidson

of the mission (through Sol 2680) Opportunity traversed the hematite plains making observations of sulfate-rich sedimentary rocks and associated hematite-concretion surface-lag (Arvidson et al., 2011; Squyres, Arvidson, Bollen, et al., 2006). These constitute the upper layers of the Late Noachian/Early Hesperian Meridiani upper etched unit and the Early Hesperian hematite unit (Hynek & Di Achille, 2017).

Opportunity began exploring the northwestern rim of Endeavour crater on Sol 2681 (August 09, 2011). Endeavour crater is a 22 km diameter complex impact structure (Figure 1a) formed in Noachian aged materials that predate the embaying sulfate-rich sedimentary rocks (Arvidson et al., 2014; Hynek et al., 2002). The Endeavour crater rim was chosen as a target because the rocks record an ancient epoch in martian history, and because phyllosilicate minerals were identified on portions of the rim from orbit (Wray et al., 2009), demonstrating that aqueous alteration is recorded in the rocks. Exploration of Endeavour crater rim directly addressed one of the main goals of the MER mission: To explore regions and associated rocks and soils where water might have been present and to make assessments regarding past habitability (Squyres et al., 2003).

Post-impact erosion has degraded the Endeavour crater rim into a series of rim segments (Grant et al., 2016; Hughes et al., 2019). Opportunity reached the rim at the ~700 m long Cape York segment that rises ~10 m above the surrounding plains (Figure 1b) (Grant et al., 2016). Near-infrared spectra from the Compact Reconnaissance Imaging Spectrometer for Mars (CRISM) instrument indicated the presence of phyllosilicates in this region (Wray et al., 2009). Investigations with the rover science payload revealed that these phyllosilicates correspond to ferric smectite occurring roughly midway down the inboard (southeastern) side of Cape York (Figure 1b; Figure L01) (Arvidson et al., 2014). (An online supplement containing locator images, Figures L01-L21, is hosted on the Open Data Repository, Mittlefehldt et al., 2021). At that location, the thin, fine-grained clastic Matijevic formation is exposed (Figure L12c); it was identified as being part of the pre-Endeavour basement and the host of the ferric smectite (Arvidson et al., 2014; Crumpler et al., 2015). Shoemaker Ridge forms the spine of Cape York and is composed of Noachian polymict impact breccias formed by the Endeavour impact; these constitute the Shoemaker formation (Crumpler et al., 2015; Squyres et al., 2012). The Grasberg formation, a thin, very-fine-grained airfall unit that drapes the lower, eroded pediment surfaces of Endeavour rim segments, also occurs on Cape York (Figure L01) (Crumpler et al., 2015; Grant et al., 2016).

Cape Tribulation is a major rim segment south of Cape York (Figure 1c). This segment also presented evidence for the localized presence of phyllosilicates, particularly in the region of a large, rim-transecting valley named Marathon Valley (Figure 1d; Figure L04) (Fox et al., 2016; Wray et al., 2009). Exploration of Cape Tribulation began at its northern tip and continued to Perseverance Valley, which cuts the rim between the southern terminus of Cape Tribulation and the next rim segment, Cape Byron (Figure 1e; Figure L09). Opportunity primarily explored rocks on the outboard (western) side of Cape Tribulation, but major science campaigns were done in Marathon and Perseverance Valleys. Both valleys cut the rim and expose bedrock of the lower stratigraphic section. Here we discuss data for all rock targets analyzed from Sol 3935 (February 17, 2015) through the last contact science measurements on Sol 5105 (June 03, 2018). We also discuss the erratic block Marquette Island which was discovered on the hematite plains on Sol 2055 (November 04, 2009). This block is interpreted to be an ejecta block of the Noachian crust that predates sedimentary rocks of the hematite plains (Arvidson et al., 2011). Soil analyses are not discussed in detail but are utilized to help interpret relationships among rock compositions.

The instruments used to investigate the geological history of the region are those of the Athena payload (Squyres et al., 2003): the Alpha Particle X-ray Spectrometer (APXS; Rieder et al., 2003), the Microscopic Imager (MI; Herkenhoff et al., 2003), the Panoramic Camera (Pancam; Bell et al., 2003) and the Rock Abrasion Tool (RAT; Gorevan et al., 2003). The MIMOS II Mössbauer Spectrometer (Klingelhöfer et al., 2003) was still operational during observations on Marquette Island; we include data from it in that discussion.

A major direction of this paper is to use compositions determined by the APXS to characterize rock types and define alteration processes. Geological context is derived from orbital and *in-situ* mapping, while Pancam images and spectra are used to interpret outcrop textures, structures, and constrain mineralogy. The micro-textures of the rocks are interpreted from MI images. The Mars observations are compared to rocks
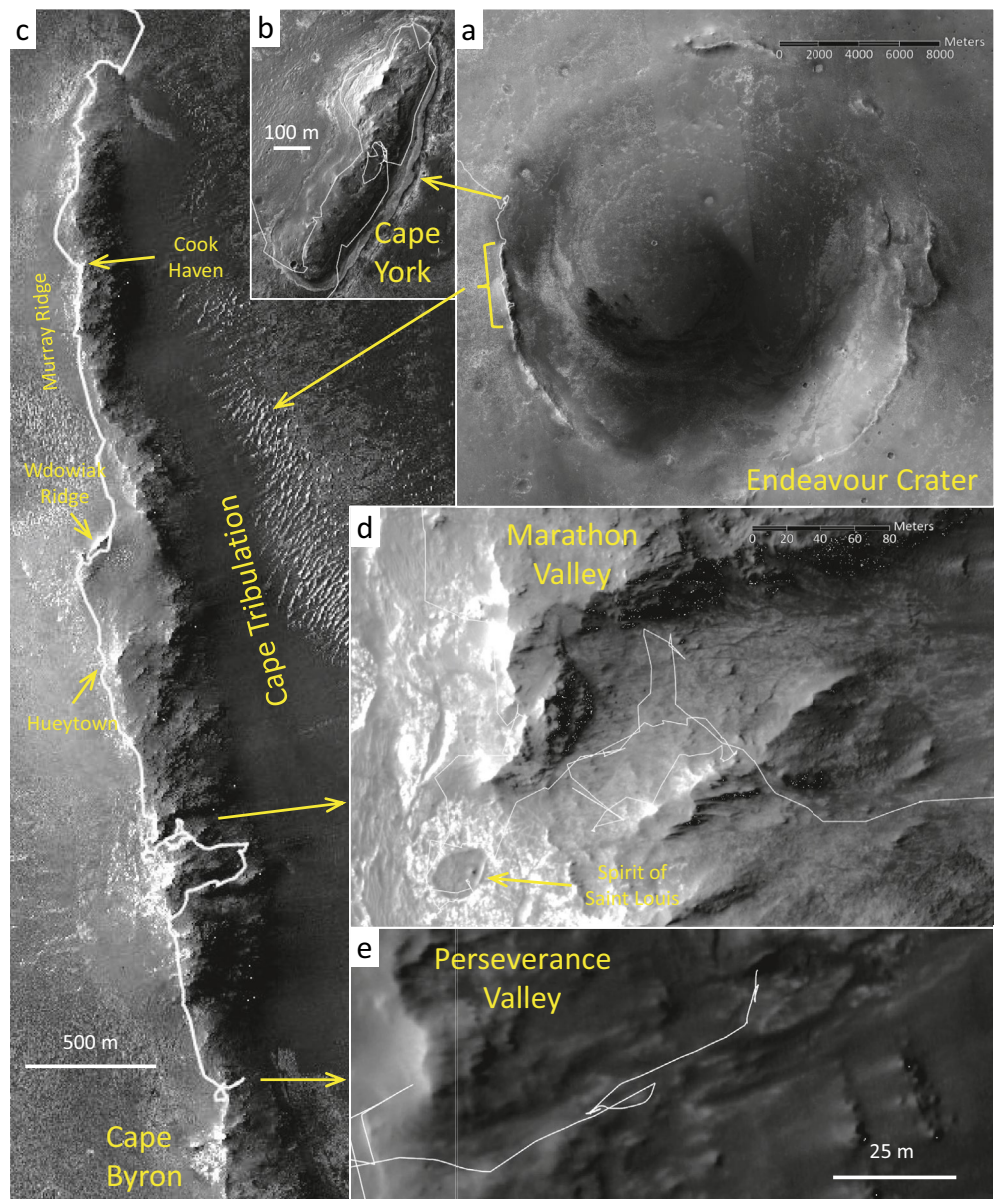
Figure 1. (a) High Resolution Imaging Science Experiment-based mosaic showing Endeavour crater. (b) Cape York. (c) The Cape Tribulation portion of the western rim showing the locations of Marathon and Perseverance Valleys. (d) Expanded view of Marathon Valley and Spirit of Saint Louis region. (e) Expanded view of Perseverance Valley region. Rover track shown in white. Images from High Resolution Imaging Science Experiment (HiRISE)-based mosaic of Endeavour crater base map (Parker et al., 2012).

from terrestrial craters and tied to information derived from cratering mechanics studies. The observations discussed here are developed into a geological and alteration history for the region around Endeavour crater.

2. The APXS Data Set

The APXS determines chemical compositions of rocks and soils using X-ray spectroscopy after irradiation with energetic alpha particles and X-rays and is a combination of the laboratory spectrometric methods of X-ray fluorescence (XRF) and particle induced X-ray emission (Rieder et al., 2003). The sample field of view has a diameter of 38 millimeters at contact which widens with increasing standoff; the instrument

response is strongest in the central region. Complete results for 287 analyses of rocks and soils from the Endeavour crater rim and 2σ precision errors of the peak areas are reported in Table 1; of these, 141 analyses were previously unpublished. (All data tables are hosted on the Open Data Repository and can be accessed through Mittlefehldt et al., 2021.) Locations for all analyses presented in Table 1 except for Marquette Island and soils far from Endeavour rim are shown in the online supplement (Figures L11–L21 of Mittlefehldt et al., 2021). Table 1 includes the typical relative accuracy, and the typical relative precision of the measurements based on a representative Shoemaker formation rock analysis, taken from Table S1 of Mittlefehldt, Gellert, et al. (2018).

The APXS data were extracted using the analysis program and calibration method described in Gellert et al. (2006), but there are some important caveats regarding the oxide results from the end of the mission. The instrument worked nominally till the end of the mission, even with progressing displacement damage by energetic neutrons in the X-ray detector. This lowered the required temperature to be significantly below −50°C at the end to get the best full-width, half-maximum (FWHM) resolution for Mn K_α of around 155 eV. Because full spectra of predetermined integration times are sequentially saved in the 12 bins of detector memory, we are able to use only those data that meet our FWHM requirements and discard the rest. Several independent aspects had a progressing negative impact on the performance that rippled through into higher uncertainties in specific elements; this has not yet been numerically assessed and is not included in the oxide table. At mission end, the ^{244}Cm source ($T_{1/2}$ = 18.1 years) had approximately 60% of its activity at landing. Degradation of the instrument deployment device limited the placement flexibility of the sensor head, often leading to increased standoff and lower geometric norm compared to contact measurements on Sol 0; this has not been considered.

The elements that are most impacted by higher standoff and lower statistics are the trace elements Ni, Zn, and Br when they are in low concentrations, typically below a few hundred µg/g. An example is target Allende (sols 5072 and 5073), which has ~15 mm standoff when the source decay is considered. Even so, the major and minor elements are reliable for this target, but the trace elements have rather high detection limits of ~100 µg/g. Additionally, Na might be lowered by a few tens of percent relative at larger standoff caused by absorption by the CO_2 atmosphere (see Gellert et al., 2006).

The typical soils were found to be very similar in composition during the long traverses of all rovers equipped with an APXS and similar at different the landing sites; these were used to check the consistency of the calibration of the instrument over time. The Opportunity instrument had a significant change in its response around sol 320, where soil data indicated loss of the 1 bar N_2 atmosphere enclosed inside the sensor head; this increased the sensitivity to low Z elements like Na by close to a factor of two. Over the course of the mission, typical soils (non-hematite enriched) were used for instrument calibration, with the last one conducted around sol 4600, indicating no further significant change in the instrument response since sol 320.

As mentioned above, the complete Opportunity APXS oxide data set presented in this work is based on the 2006 calibration and has not yet been tweaked for comparison with the APXS data from other missions or other instruments landed on Mars. The remaining uncertainties in cross calibration described in Gellert et al. (2006) will be addressed in future work. The principles of the APXS method, where elemental concentrations are extracted from their characteristic peak areas with corrections for self-absorption (typically on the order of ~10%), makes the data set ideal for statistical analysis of element groups to distinguish geological formations.

3. Geological Context

The basement in the region explored by Opportunity consists of the Early to Middle Noachian subdued cratered unit (Hynek & Di Achille, 2017) which is interpreted to be composed of primary (volcanic, pyroclastic) and secondary (impact breccia, fluvial and aeolian sedimentary) lithic types (Hynek & Di Achille, 2017). It is overlain by three Meridiani etched plains units of Middle/Late Noachian to Late Noachian/Early Hesperian in age (Figure 2). They are interpreted to be aeolian and/or volcanic deposits (Hynek & Di Achille, 2017; Hynek & Phillips, 2008). The Burns formation is the uppermost lithified section of the etched unit stratigraphy, and is sulfate-rich aeolian sandstone (e.g., Grotzinger et al., 2005; Squyres & Knoll, 2005; Squyres, Arvidson, Bollen, et al., 2006).
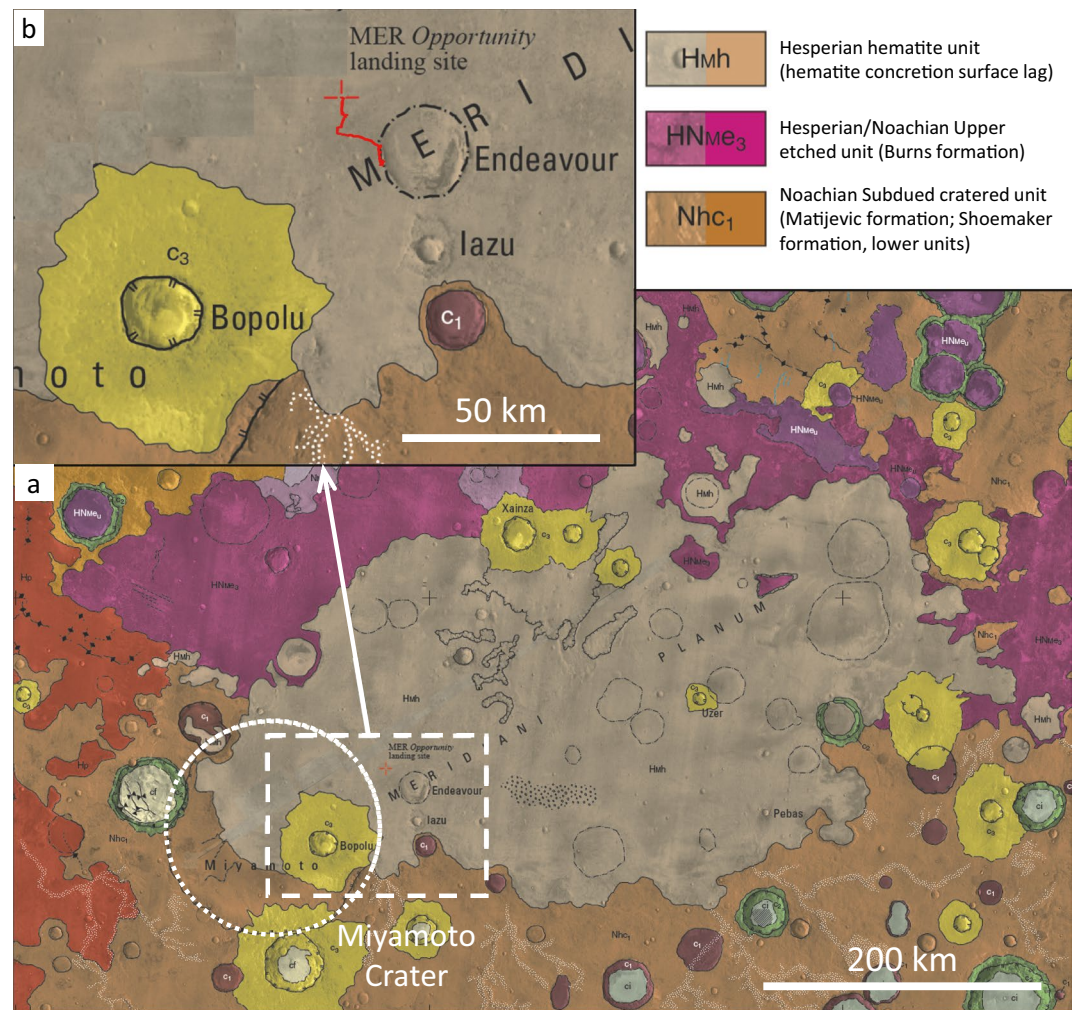
Figure 2. Portions of the geological map of Meridiani Planum showing the relationships between the Noachian subdued cratered unit, the Noachian/Hesperian upper etched unit and the Hesperian hematite unit in the vicinity of the Opportunity traverse (red squiggly line in [b]). The legend shows geologic units discussed here with the rover-based units identified; all other unit symbols are defined in Hynek and Di Achille (2017); the map is modified from that source.

Endeavour crater is northeast of the ~160 km-diameter Miyamoto crater (Grant et al., 2016; Newsom et al., 2003) which is in the subdued cratered unit (Figure 2a). Miyamoto crater is an ancient, degraded crater partially filled by Meridiani etched plains units on the north-northeast side. Morphologic evidence points to fluvial erosion having impacted the landscape outside and inside the crater (Newsom et al., 2003, 2010), and Fe-Mg-rich smectite phases are located on the western floor of the crater (Wiseman et al., 2008). Bopolu crater, 19 km in diameter, impacted on the Meridiani etched plains units that partially fill Miyamoto crater. This relatively pristine crater exposes altered Noachian basement in its walls (Grant et al., 2016), further testifying to ancient alteration of the Miyamoto crater floor rocks. Alteration in this region was engendered by the hydrological environment of western Arabia Terra in which ground waters from the southern highlands emerged in local topographic lows and caused alteration of the bedrock (Andrews-Hanna & Lewis, 2011; Andrews-Hanna et al., 2007). The Endeavour impact occurred ~20 km outside the rim of Miyamoto crater within the region of its continuous ejecta deposit. The pre-impact terrain would have included polymict breccias from that earlier impact and these could have been altered as observed for floor rocks in Miyamoto crater (Wiseman et al., 2008). Iazu crater, 6.8 km-diameter structure ~25 km south of Endeavour crater (Figure 2b), is a relatively pristine, simple bowl-shaped crater surrounded by a pedestal of ejecta. That latter is thought to be the result of wind erosion preferentially removing the less resistant Burns formation rocks

(Powell et al., 2017). Iazu crater exposes Noachian-aged, ferric-smectite-bearing altered basaltic-composition basement below Burns formation in its crater walls (Powell et al., 2017), further establishing that the pre-impact terrain for Endeavour crater consisted of ancient, altered rocks.

The rover-defined stratigraphy of the region is divided into four formations which are, oldest to youngest; the Matijevic, Shoemaker, Grasberg and Burns formations (Crumpler et al., 2015). The Matijevic formation is part of the pre-Endeavour terrain exposed at the inboard side of Cape York (Figure L01), and is a fine-grained clastic rock (Arvidson et al., 2014). The limited exposures hamper conclusions regarding its origin, but its morphology and texture are consistent with formation as volcanic ash or distal impact ejecta (Crumpler et al., 2015). Polymict impact breccias of the Shoemaker formation comprise the major lithic type of the Endeavour crater rim on the segments explored by Opportunity and underpin the topographic expressions of the rim segments (Crumpler et al., 2015; Squyres et al., 2012). The Shoemaker formation, the major focus of this communiqué, is discussed in Section 4. A continuous bench of bright rock encircles Cape York (Figure L01), partially surrounds the margin of Cape Tribulation and is discernable in High Resolution Imaging Science Experiment (HiRISE) images of other rim segments of Endeavour crater (e.g., Grant et al., 2016). This bench is part of the Grasberg formation, a very-fine-grained clastic deposit that drapes the eroded lower slopes of rim segments (Crumpler et al., 2015). The Grasberg formation is a thin, altered airfall deposit that is of volcanic or impact origin and might be regional in extent (Crumpler et al., 2015). New analyses of two Grasberg formation rocks are included in Table 1, but we do not discuss them; the composition of this formation is discussed in Mittlefehldt, Gellert, et al. (2018). The Burns formation is dominated by sulfate-rich sandstones (e.g., Edgar et al., 2012; Grotzinger et al., 2005). Most of the sandstones are aeolian in origin, but there are some aqueous facies that bespeak local fluvial reworking and rare mudstones indicate localized deposition in quiet water, possibly a lacustrine setting (Edgar et al., 2012, 2014; Grotzinger et al., 2005, 2006; Hayes et al., 2011). Unconformities separate all formations.

Several lithic types do not occur as mappable formations that are covered here under the rubric "dark rocks." These include dark-rock boulder-float similar to those discussed previously (Mittlefehldt, Gellert, et al., 2018), two types of scattered, more massive, fine-grained rock that we refer to as blue- and purple-rock erratics based on their appearance in Pancam false color images, and three types of dark rock from Perseverance Valley. Finally, we encountered a dark-rock block—Marquette Island—on the hematite plains roughly 11,800 meters from the Endeavour rim. Marquette Island is interpreted to be an ejecta fragment from the Noachian crust (Arvidson et al., 2011), and has a general compositional similarity to Adirondack-class basalts from Gusev crater but contains a higher fraction of light elements (H, C, O) than found for other rocks (Mittlefehldt et al., 2010). Because this might indicate unusual alteration, we discuss it here.

4. Shoemaker Formation

Shoemaker formation rocks are polymict impact breccias found on the rim of Endeavour crater which we have interpreted as being ejecta from the crater (Arvidson et al., 2014; Crumpler et al., 2015; Mittlefehldt, Gellert, et al., 2018; Squyres et al., 2012). The first exposures of Shoemaker breccias encountered by Opportunity were not in contact with other units, and we equated them with impact suevite (Squyres et al., 2012). Later we discovered exposures that are lying directly on the pre-Endeavour Matijevic formation (Arvidson et al., 2014), which is inconsistent with being a suevite-equivalent deposit. Suevite is a late deposit in cratering events and overlies allogenic breccias formed during the impact process, inside and outside the crater (e.g., Dressler & Reimold, 2001; Masaitis, 1999; Stöffler et al., 2013). Thus, we reinterpreted the Shoemaker formation as being ballistically emplaced ejecta, equivalent to the Bunte Breccia at the Ries crater (Mittlefehldt, Gellert, et al., 2018). Subsequent investigations in Marathon and Perseverance Valleys presented evidence that some subunits of the Shoemaker formation pre-date the Endeavour impact (Mittlefehldt, Crumpler et al., 2018; Mittlefehldt, Arvidson et al., 2019). We present that evidence in this section and refine our interpretation of the Shoemaker formation. We present our compositional information on Shoemaker formation rock targets and discuss them in relation to our interpretation of subunit origins. Further, we discuss alteration features in the Shoemaker formation from Marathon and Perseverance Valleys, and compositional differences between surfaces and interiors of several rocks. Locator images for all Pancam images shown and all rock targets analyzed are presented in Mittlefehldt et al. (2021).
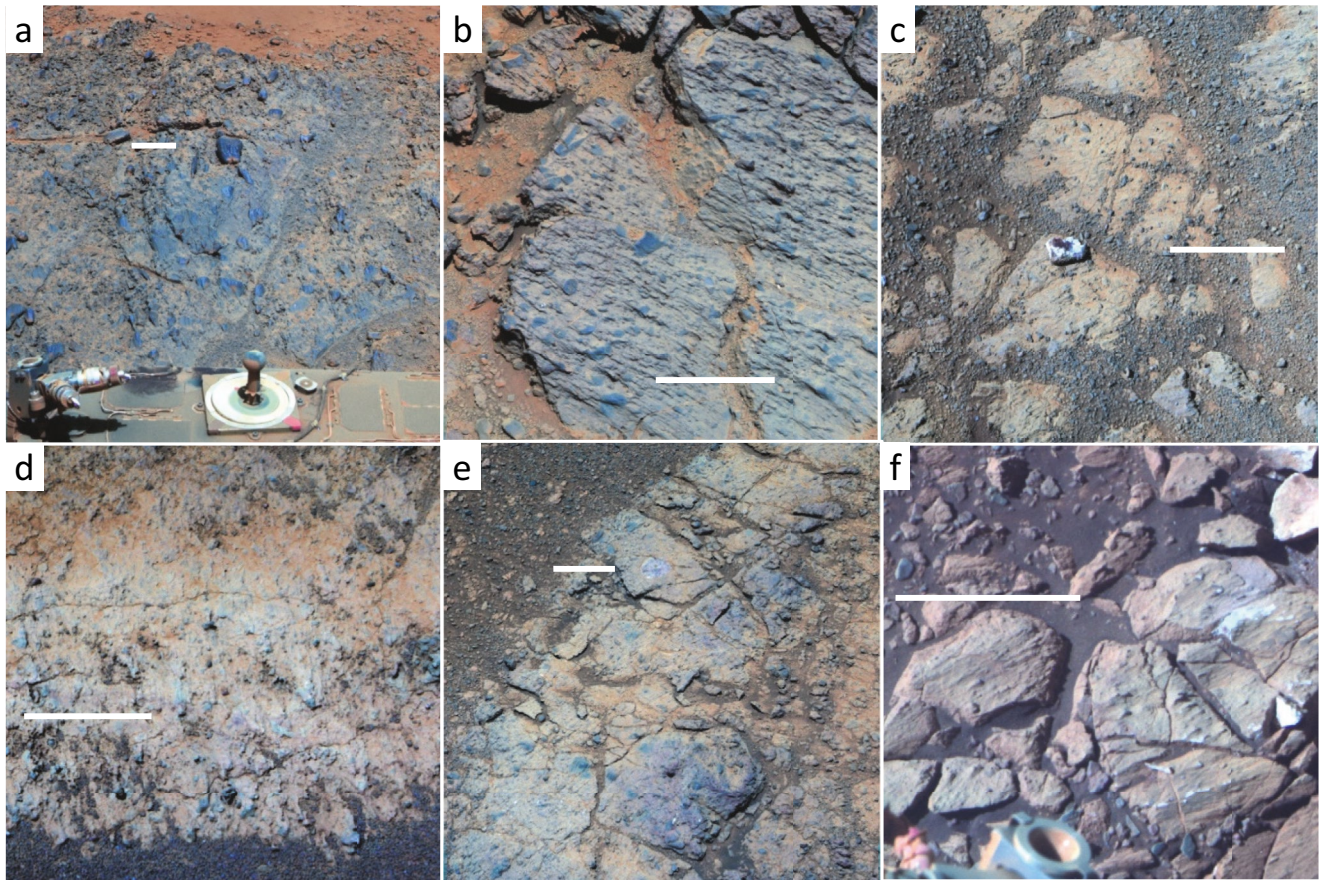
Figure 3. Pancam false-color images showing examples of macrotextures of Shoemaker formation outcrops: (a) Boesmanskop and Komati (clast), Greeley Haven member on Cape York (Sol 2795); (b) Moreton Island, upper Shoemaker formation on Murray Ridge, Cape Tribulation (Sol 3494); (c) Cape Elizabeth (outcrop block), upper Shoemaker, and Pinnacle Island (lose rock) in Cook Haven, Cape Tribulation (Sol 3540); (d) Thermopylae, lower-2 Shoemaker at Spirit of Saint Louis, Cape Tribulation (Sol 3998); (e) Smectite-rich outcrop, lower-1 Shoemaker in Marathon Valley (Sol 4419); (f) Mesilla, lower Shoemaker in Perseverance Valley (Sol 4880). False color rendered using Pancam left-eye filters 2, 5, and 7 centered on 753, 535, and 432 nm (hereafter L257). Scale bars are ~10 cm at the locations shown. The locations of these rocks can be found in Mittlefehldt et al. (2021), Figures L02 through L04 and L09.

4.1. Stratigraphy, Texture, Morphology, and Origin of Subunits

The Shoemaker formation is the major rock unit of the rim. It originally formed the continuous ejecta deposit surrounding Endeavour crater, but subsequent degradation has reduced its areal coverage (Grant et al., 2015). It is divided into three members on Cape York (Figures 15 and 17 of Crumpler et al., 2015). Copper Cliff is the lowermost member and unconformably overlies the pre-impact Matijevic formation (Figure L01) (Crumpler et al., 2015). It is a transitional breccia that shows some textural and compositional characteristics of the underlying Matijevic formation (Arvidson et al., 2014; Crumpler et al., 2015; Mittlefehldt, Gellert, et al., 2018). Mittlefehldt, Gellert, et al. (2018) concluded that the Copper Cliff member was formed by mixing Endeavour ejecta with material eroded from the pre-impact paleosurface via a ballistic erosion-sedimentation process (e.g., Hörz et al., 1983; Oberbeck, 1975). The Chester Lake member, the middle of the three, was encountered on the southern tip of Cape York when we began exploring the rim (Figure L01) (Crumpler et al., 2015). The Greeley Haven member is the thickest and uppermost subunit of the Shoemaker formation, and is a coarse, clast-rich polymict breccia with multi-cm-sized dark clasts in a brighter, fine-grained matrix (Figure 3a) (Arvidson et al., 2014; Crumpler et al., 2015; Mittlefehldt, Gellert, et al., 2018; Squyres et al., 2012).

The Shoemaker formation is subdivided into upper and lower subunits on Cape Tribulation; no attempt was made to correlate them with the three members defined on Cape York. Most of the breccias on Cape Tribulation discussed in Mittlefehldt, Gellert, et al. (2018) are morphologically and texturally like

the Greeley Haven member on Cape York (e.g., Figure 3b); these are upper Shoemaker rocks (Crumpler et al., 2019, 2020). The area around the Spirit of Saint Louis feature and the floor of Marathon Valley contain breccias that have lower abundances of clasts and typically smaller clasts (Figures 3d and 3e), which are mapped as two subunits (lower-1 and lower-2) of the Shoemaker formation (Crumpler et al., 2019, 2020). Previously we noted that breccias at Cook Haven and at the Hueytown fracture zone (see locations, Figure 1c) showed some similarity to breccias now mapped as lower-1 and lower-2 Shoemaker in Marathon Valley (Figure 3c) (Mittlefehldt, Gellert, et al., 2018). A single lower subunit of the Shoemaker formation is recognized in Perseverance Valley (Figure 3f) (Crumpler et al., 2019, 2020).

We now identify the lower Shoemaker formation subunits as distal impact ejecta from at least two pre-Endeavour craters, and thus they are not correlative with the Shoemaker formation on Cape York. The arguments supporting this are based on comparing upper and lower Shoemaker rocks with experimental and observational studies of impact processes (Oberbeck, 1975) plus studies of terrestrial caters (e.g., Hörz et al., 1983; Mader & Osinski, 2018; Maloof et al., 2010; Shoemaker, 1963).

Impacts produce a variety of rock types from parautochthonous cataclastic breccias in the crater floor/walls and central uplift (in larger craters) to allochthonous breccias and impact-melt rocks on the crater floor and dispersed outside the crater on the rim (e.g., Grieve & Therriault, 2004; Osinski et al., 2011). Two types of deposits occur at craters: allochthonous impact breccias form a lower layer, and impact-melt breccias (e.g., suevite) form an upper layer (Osinski et al., 2011); these are found outside and inside the crater rim but here we are concerned with exterior deposits. This basic two-tier structure is found at craters on the terrestrial planets and the Moon (Osinski et al., 2011). Several hypotheses have been advanced to explain the Ries suevite deposits, but recent work demonstrates that the suevite deposits are like ignimbrites in texture and morphology (Siegert et al., 2017); these authors posit that the suevite was formed from radial, granular fluid–based density currents produced early in the excavation stage of the Ries. Nevertheless, suevite overlies the ballistically emplaced Bunte Breccia.

Fresh craters on Mars often have surrounding ejecta deposits with two or more layers, often called rampart craters (Barlow, 2005, 2010). Two main hypotheses have been advanced to explain layered ejecta deposits—fluidization by melted ground ice (Carr et al., 1977) and atmospheric drag acting on the finer particles in the ejecta curtain (Schultz & Gault, 1979)—but other mechanisms have also been suggested (see Weiss & Head, 2017). The evidence indicates that the upper layers are formed from ground-hugging surficial flows (Baloga et al., 2005). In the case of the atmospheric drag hypothesis, the lower layer near the crater rim consists of ballistically emplace ejecta and finer material would form the upper layer (Schultz & Gault, 1979; and see Melosh, 1989, Section 6.3.5). Fluidization by melted ice (Carr et al., 1977) would result in a fluidized debris flow (Melosh, 1989, p 100); debris flows are typically poorly sorted and unstratified (e.g., Chen et al., 2008). There is no evidence to support formation of the two-tier stratigraphy with lower, finer and upper, coarser breccias at a single crater even if Endeavour crater produced a layered ejecta deposit. As discussed above, Shoemaker formation breccias directly overlie the pre-Endeavour-impact clastic rocks of the Matijevic formation on the rim, and thus are allochthonous breccia ejected from Endeavour crater. As summarized by Oberbeck (1975), ejecta fragments from an impact are launched at differing angles and velocities, but all follow ballistic trajectories. The earliest ejecta fragments are derived from closer to the pre-impact surface, nearer the impact point, and are launched at the highest angles and velocities (Figure 4). Conversely later ejecta fragments are generally derived from deeper in the target zone, further from the impact point, and are launched at lower angles and velocities. This results in a conical ejecta curtain that sweeps outward, first along with the growing transient crater margin and then over the pre-impact surface once the final transient crater size is reached. As the ejecta curtain moves outward the largest and slowest fragments are at its base, the fastest and smallest ones at its top. Close to the transient crater rim, fragments impact the surface at shallower angles, lower velocities and fragment sizes are larger on average than is the case for the distal edge of the ejecta deposit (solid arrow—schematic ejecta fragment velocity vectors; Figure 4 insets). Furthermore, the impacting ejecta fragments cause ballistic erosion and sedimentation on the pre-impact surface resulting in mixing pre-impact rock with ejected clasts. This process is more effective at greater distances because of the steeper impact angles and higher velocities of the ejecta fragments. The final dregs of energy are dissipated through outward, ground-hugging flow of the mixture of ejecta fragments and eroded bedrock/soil (open arrow—schematic ejecta deposit velocity vectors; Figure 4 insets).
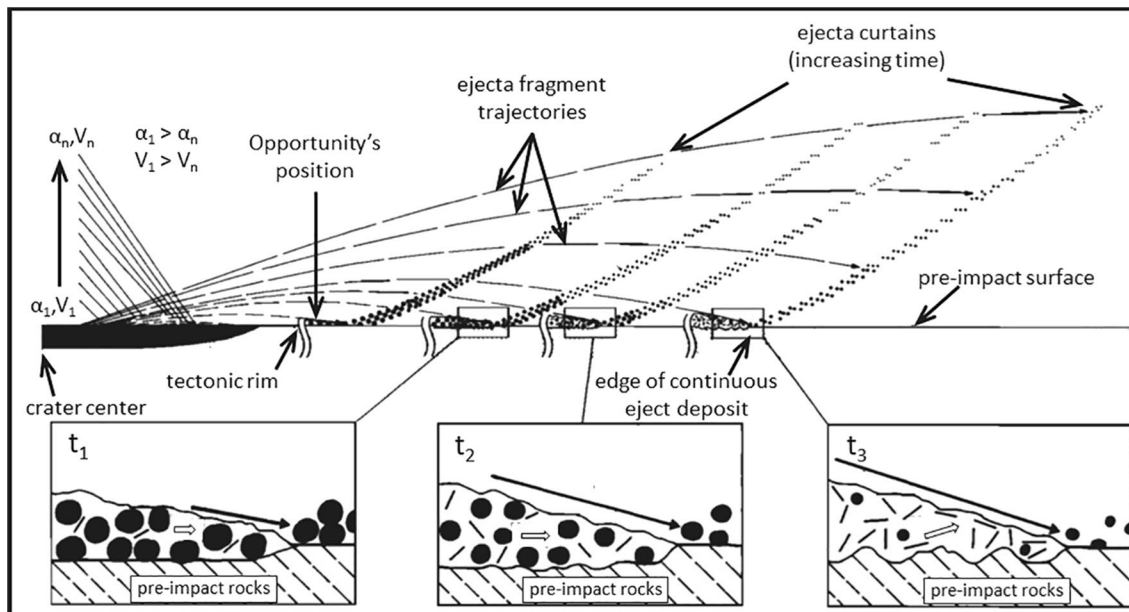
Figure 4. Schematic diagram of ejecta emplacement outside a complex crater, after Oberbeck (1975). Insets show the area at the base of the ejecta curtain at three different times; solid arrows show schematic vectors of ejecta fragment motion; open arrows show schematic vectors of ejecta deposit motion. α - ejection angle; V–ejection velocity.

The results are polymict breccias that have larger average clast sizes and lower matrix contents close to the tectonic rim of a large crater than at the distal edge of the ejecta deposit.

Detailed geological work on terrestrial craters, especially the extensive studies of the Bunte Breccia of the Ries Crater, offer specific examples of ejecta deposits that match the synopsis presented by Oberbeck (1975). The Ries Crater is of similar size to Endeavour crater, ~26 km diameter versus ~22 km, is well-preserved and thus is an excellent terrestrial analog. Hörz et al. (1983) summarized petrologic work done on cores taken at different locations and radial ranges through the Bunte Breccia and noted that there is no systematic vertical trend in the grain sizes of matrix components or clast size. The cores are chaotic mixtures of clasts and matrix throughout their length at any given location. Mader and Osinski (2018) similarly noted that the polymict breccias of the ~28 km diameter Mistastin Lake impact structure are poorly sorted, and Shoemaker (1963) described the ejecta surrounding the simple, bowl-shaped, 1.2 km diameter Meteor Crater as consisting of unsorted debris from <1 μm to >30 m in size. Hörz et al. (1983) identified a systematic trend of decreasing average clast size with radial distance from the Ries Crater rim, and Shoemaker (1963) reported decreasing block size and frequency with increasing radial range from Meteor Crater. Hörz et al. (1983) do not specifically state that the clast/matrix ratio decreases with radial range, but this can be inferred from the observations that: (a) the amount of primary crater material in the ejecta decreases with radial range; and (b) the matrix is >95% derived from ballistic erosion of the local surface. Thus, the geological evidence demonstrates that ejecta deposits are unsorted, chaotic breccias at individual locations that show systematic variations with radial range.

The textures of the upper and lower Shoemaker formation do not match those expected of ejecta from a single impact. We have the best stratigraphic control on Cape Tribulation in the region of Marathon Valley where the two lower subunits occur as the valley floor and around the Spirit of Saint Louis feature, while upper Shoemaker rocks form the bounding ridges (Figure 5) (Crumpler et al., 2020). In Perseverance Valley the upper Shoemaker similarly overlies the lower Shoemaker (Crumpler et al., 2020). A systematically finer-grained and clast-poor breccia at the base of a coarser-grained, clast-rich breccia is inconsistent with formation as an ejecta deposit from a single impact event. Rather, the textures of the lower Shoemaker subunits are consistent with formation from impacts that were more distant than that which produced the upper Shoemaker. Hence, the geologic evidence supports an origin of the lower Shoemaker subunits on
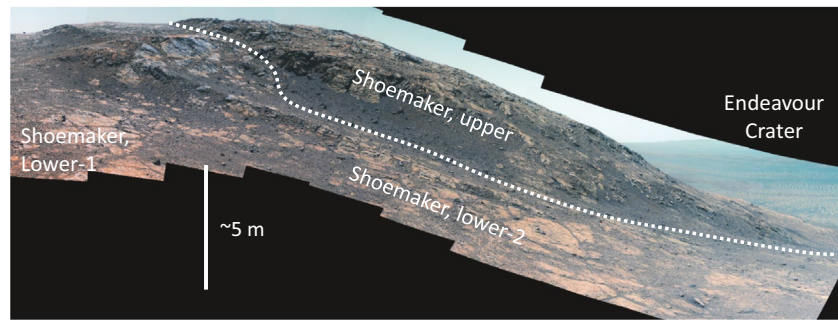
Figure 5. Pancam false-color image (Gibraltar II panorama, L257) showing the contact between the upper and lower units of the Shoemaker formation in Marathon Valley. Images acquired between Sols 4446–4453. The location of this image can be found in Mittlefehldt et al. (2021), Figure L07.

Cape Tribulation as distal ejecta from at least two impacts that predate Endeavour crater formation; the ridge-forming upper Shoemaker is a proximal ejecta deposit from the Endeavour impact.

On Cape York, the Copper Cliff member of the Shoemaker formation overlies the pre-impact Matijevic formation and was mapped as a transitional breccia (Crumpler et al., 2015). The Copper Cliff member shows some textural and compositional similarities to the Matijevic formation (Crumpler et al., 2015; Mittlefehldt, Gellert, et al., 2018), which we attributed to ballistic erosion and sedimentation processes as the Endeavour ejecta impacted the pre-impact surface (Mittlefehldt, Gellert, et al., 2018). Although mapped as a transitional breccia, the Copper Cliff member is nevertheless a coarse breccia, the transitional character being imparted by inclusion of 1–2 mm spherules like those that are present in the Matijevic formation (Arvidson et al., 2014; Crumpler et al., 2015). Thus, the geological evidence does not support a pre-Endeavour origin for the Copper Cliff member, and all Shoemaker formation breccias on Cape York are Endeavour deposits.

4.2. Composition

We have done 138 analyses of Shoemaker formation targets representing 68 different rocks (this work; Mittlefehldt, Gellert, et al., 2018). Of these, 29 analyses were done on brushed targets, while 18 were on abraded targets. For some of the latter the abrasion was of low quality, either because the activity faulted-out before completion, or topography of the surface was too great to result in a good abrasion circle at the planned depth. We consider that 13 analyses were on well-abraded targets.

We have grouped the Shoemaker formation APXS targets according to geologic map units (Table 1) (Crumpler et al., 2015, 2020); their geographic locations are noted on the table. A region mapped as Shoemaker lower-1 in Marathon Valley presented spectral evidence for the presence of Fe-Mg smectite in CRISM data (Fox et al., 2016), and four analyses from the region showing the strongest smectite signal are grouped separately. The Parral target is an ~5 cm rock fragment in a region of bedrock fragments on a dark sand substrate. The Zacatecas target from this region consists of mixed small bedrock fragments and dark sand. Both are listed with the upper Shoemaker rocks, but the latter might better be considered a composite soil (see Cabrol et al., 2014), and Parral is plausibly a cobble of lower Shoemaker (see below).

Shoemaker formation rocks are broadly basaltic in composition and similar to an estimated mean martian crust composition (Taylor & McLennan, 2009) (Figure 6). Compositional variations within the suite generally are minor. Compositions of breccias from different locations and/or subunits substantially overlap for many elements, but there are nevertheless systematic differences for some elements. Thus, on Cape York the average FeO content increases in the sequence Copper Cliff, Greeley Haven, Chester Lake members, and Shoemaker formation rocks have systematically higher Fe/Mn on Cape Tribulation than on Cape York (Mittlefehldt, Gellert, et al., 2018). Most of the compositional differences observed among subunits of the Shoemaker formation are in the volatile elements (S, Cl, Br; Figure 7) that have been labile in the recent Martian environment (see Mittlefehldt, Gellert, et al., 2019, and references therein), and in the mobile elements (P, Mn, Ni, Zn) that were mobilized by localized alteration events (Arvidson et al., 2016; Jolliff et al., 2019; Mittlefehldt, Gellert, et al., 2018, 2019). Table 2 gives the mean compositions for subunits of
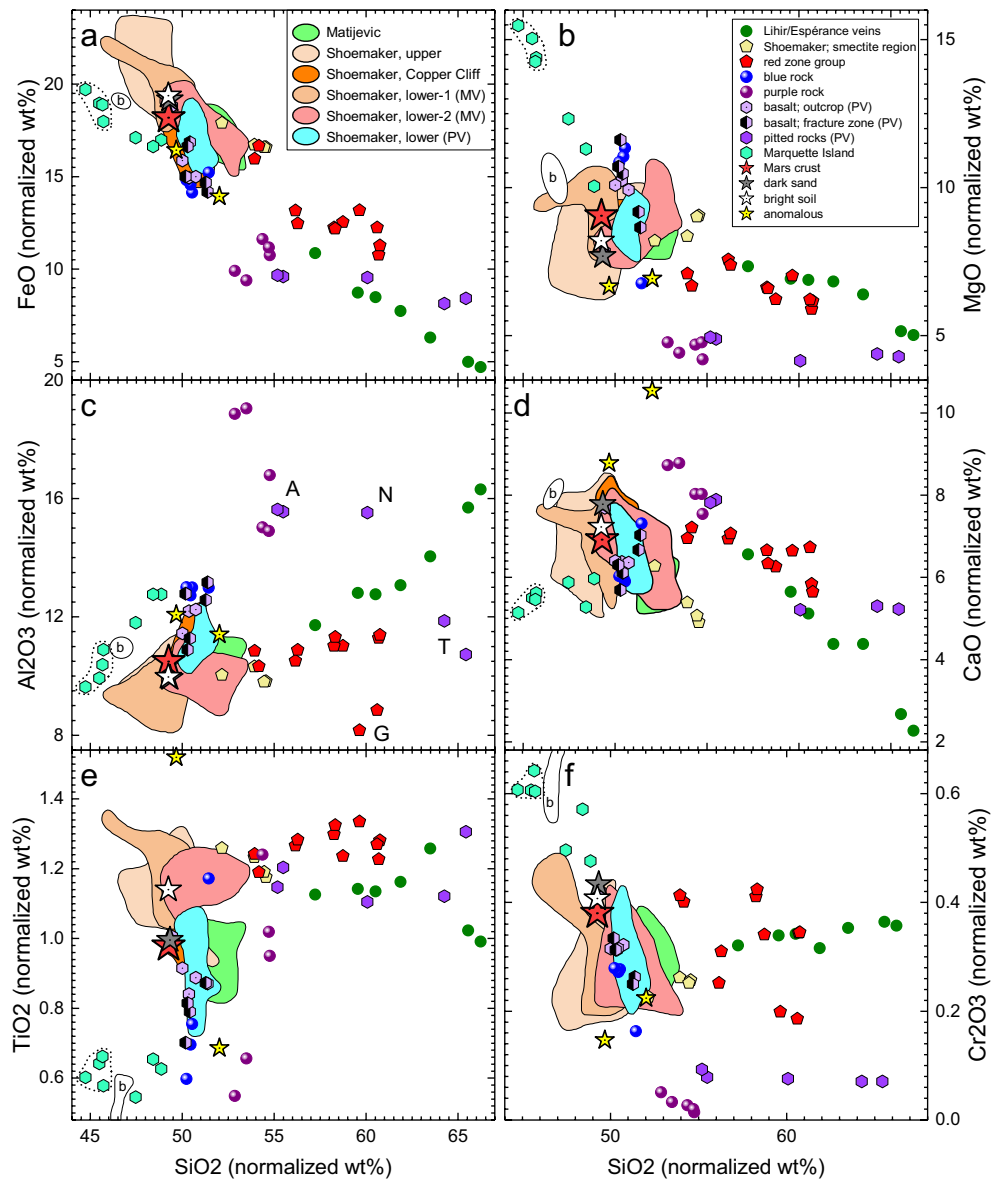
Figure 6. Element versus SiO$_2$ diagrams for Endeavour crater rim rocks, normalized to a SO$_3$−, Cl− and Br-free basis. Anomalous targets are Sledge Island1 and Sarcobatus Clast 2; see text. Labeled points in (c) are: A–Allende; G–Gasconade; N–Nazas; T–Tomé. Dotted field encloses the abraded targets of Marquette Island. White field labeled b is abraded targets of Adirondack-class basalts from Gusev crater. Locations of Allende, Nazas and Tomé (pitted rocks) can be found in Mittlefehldt et al. (2021), Figure L10; that of Gasconade in Figure L06; and those of Sledge Island1 and Sarcobatus Clast 2 in Figure L03.

the Shoemaker formation. As-measured compositional data are averaged for the three volatile elements; for all other elements, the analyses are normalized to a SO$_3$-, Cl- and Br-free basis, and the normalized data are averaged. Excluding the volatile elements, the averages of different subunits for most of the elements overlap within uncertainty.

Because variations in composition within the Shoemaker formation are subtle, multivariate statistical techniques offer the best method for revealing compositional associations. We used Agglomerative Hierarchical Cluster Analysis (AHCA) to group observations (APXS targets) by similarities in variables (elements). Details of the AHCA modeling are presented in a file hosted on the Open Data Repository (Mittlefehldt et al., 2021). The modeling included all rock types formed before or during the Endeavour impact, apart
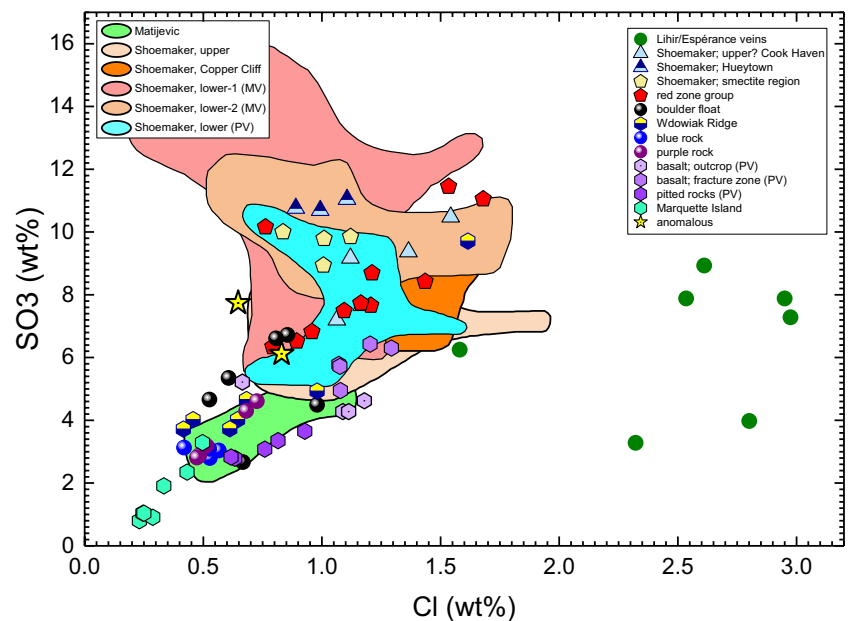
Figure 7. Plot of SO$_3$ versus Cl for Endeavour crater rim rocks.

from targets in the Matijevic formation, Shoemaker formation and red-zone group that contained CaSO$_4$ veins. Soils were included to help evaluate the effects partial soil cover might have on the compositions of untreated surfaces. This resulted in 237 analyses being modeled; Table 3 gives the element/Si mole ratios for analyses used in the modeling.

The volatile elements S, Cl and Br were excluded from the analyses because we are focusing on the silicate compositions. Sulfur and Cl contents are variable and at wt% concentration levels (Table 1; Figure 7); inclusion of these elements in the modeling would cause targets with very similar silicate compositions to occupy dissimilar clusters. The mobile elements P, Mn, Ni and Zn were included in the first model run to help evaluate which targets might contain subtle signatures of alteration processes; a second model excluded these elements to evaluate the impact of alteration.

We required the models to return 20 clusters to obtain fine granularity on the results; clusters were merged at higher levels by inspection of the dendrograms to yield geologically interpretable results. A cluster hierarchy matrix summarizing the distributions of different rock types in the clusters for the first model run is given in Table 4a; that for the second model run is in Table 4b. A series of detailed dendrograms for the models are given in material hosted on the Open Data Repository (Figure M01–M15, Mittlefehldt et al., 2021). Inspection of these showed that there are four major clusters in each of the models; simplified dendrograms showing these major clusters are presented in Figure 8.

The four major clusters of the first model are: A, including clusters 1–7 (72 analyses); B, containing clusters 8–11 (40 analyses); C, consisting of clusters 12–15 (91 analyses); and D, composed of clusters 16–20 (34 analyses) (Figure 8a and Table 4a). Major cluster D links with ABC at a distance of 27.7, more than twice the distance of the A-BC linkage (12.3). Major cluster D includes most analyses (63%) of the four silica-rich lithic types shown in Figure 6: silica-rich boxwork veins from the Matijevic formation; the red-zone group; pitted rocks from Perseverance Valley; purple-rock erratics (Table 4a; Figure M08). These will be discussed in Section 4.3. All analyses of erratic rock Marquette Island are in cluster 15 of major cluster C (Table 4a; Figure M07); this rock is discussed in Section 5. For the second AHCA model run, the four major clusters are: I, including clusters 1–3 (49 analyses); II, containing clusters 4–10 (124 analyses); III, consisting of clusters 11–13 (38 analyses); and IV, composed of clusters 14–20 (26 analyses) (Figure 8b and Table 4b) (Roman numerals are used for clarity in the discussion). The distance of the linkage separating major cluster IV from the other is ~12.4, less than half the distance of the ABC-D linkage in the first model run (Figure 8), which indicates that the mobile elements contribute importantly to the compositional variability.
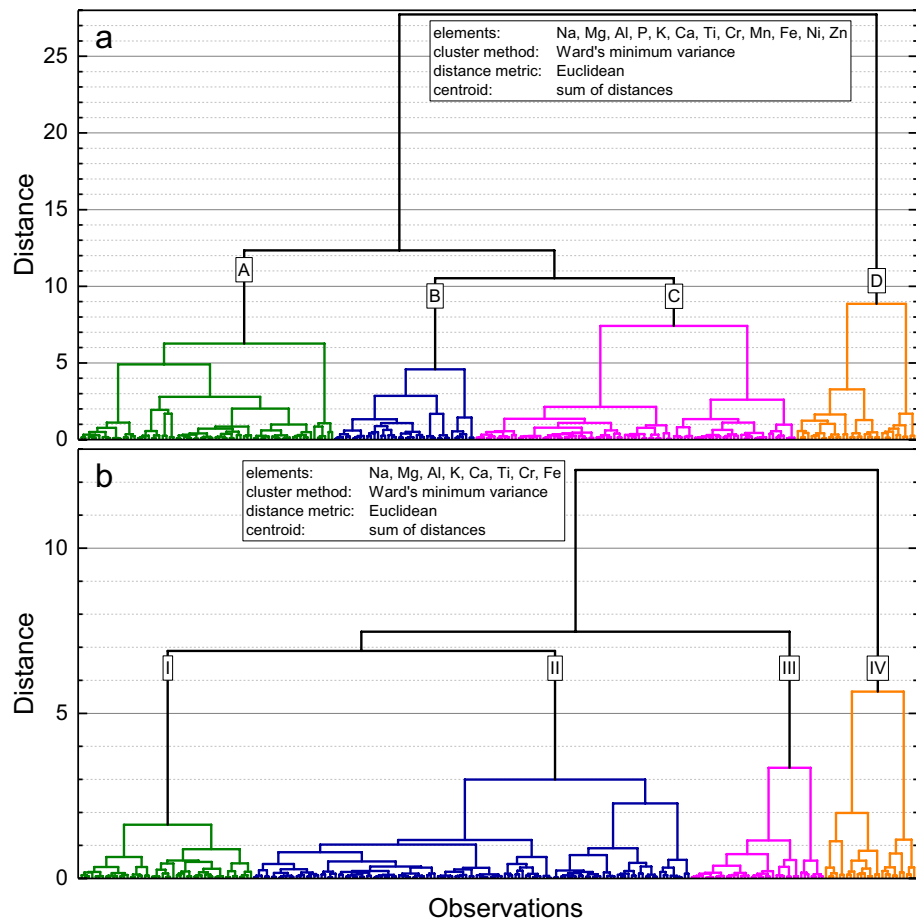
Figure 8. Simplified dendrograms of Agglomerative Hierarchical Cluster Analysis (AHCA) of Endeavour crater rim rocks and soils to show the four major clusters resulting from the first (a) and second (b) model runs. The methodology of the modeling and detailed dendrograms are given in Mittlefehldt et al. (2021).

All soil targets in the first model occupy either cluster 6 or 14 (Table 4a) and most of the soil targets in the second model are in cluster 11 (Table 4b). All rock targets in these clusters are untreated. Because of this, we consider their compositions to be possibly compromised and they are discounted in the discussion that follows. Six untreated rocks are clustered with soils in both model runs and are especially suspect.

For the first model, analyses contained in major cluster A include 65% of the Endeavour crater Shoemaker breccias, but none of the pre-Endeavour crater Shoemaker breccias. It includes 57% of the Matijevic formation rocks (excluding the boxwork veins), 20% of the dark basaltic rocks and 18% of the erratic rocks (Table 4a). Analyses contained in major cluster B include 6% of the Endeavour crater Shoemaker formation breccias, 33% of the pre-Endeavour Shoemaker breccias, the remainder of the Matijevic formation rocks, and none of the dark basaltic or erratic rocks. Major cluster C includes 27% of the Endeavour crater Shoemaker breccias, 64% of the pre-Endeavour Shoemaker breccias, none of the Matijevic formation analyses, 13% of the dark basaltic rocks and 41% of the erratic rocks. Major cluster D includes only 3% of the pre-Endeavour Shoemaker breccias, none of the Matijevic formation analyses, 67% of the dark basaltic rocks and 41% of the erratic rocks. The sole Endeavour crater Shoemaker breccia analysis in major cluster D is the anomalous target Sledge Island1.

There is a substantially different distribution of Endeavour and pre-Endeavour Shoemaker formation breccias between the major clusters; most Endeavour Shoemaker breccias are in major cluster A while most pre-Endeavour Shoemaker breccias are in major cluster C. There is a geographic distinction for clustering amongst Endeavour crater Shoemaker breccias: 97% of those from Cape York are in major cluster A while

68% of those from Cape Tribulation are in major cluster C. This latter fact suggests either that there was a different lithic mixture in the ejecta deposited on Cape York than on Cape Tribulation or that alteration processes on the two rim segments were different. The latter is supported by the second AHCA model that excluded the mobile elements. In this model, Endeavour crater Shoemaker breccias from Capes York and Tribulation are all dominantly (86%–89%) in major cluster II (Table 4b). We conclude that post-Endeavour alteration processes in the region of Cape York were different in degree or style than those on Cape Tribulation. We presaged this possibility in Mittlefehldt, Gellert, et al. (2018) where we noted that there was a systematic difference in Fe/Mn ratios of Shoemaker formation breccias between those on Cape York and on Murray Ridge from Cape Tribulation, and we noted than Mn was mobile during alteration.

When the mobile elements are excluded from the model, pre-Endeavour Shoemaker breccias are mostly in major cluster II with the Endeavour crater Shoemaker breccias (Table 4b). However, the pre-Endeavour Matijevic formation rocks are overwhelmingly in major cluster I. Together, these results suggest that the Shoemaker breccias deposited by the Endeavour impact are mostly composed of lithic materials like the lower Shoemaker, and rocks like the Matijevic formation make up a minor proportion.

There are some textural similarities between the Copper Cliff member of the upper Shoemaker and the Matijevic formation that are not observed for other members of the Shoemaker formation on Cape York (Crumpler et al., 2015). Our previous AHCA modeling indicated a compositional connection between the Copper Cliff member and the Matijevic formation that was not observed for other members of the Shoemaker formation (Mittlefehldt, Gellert, et al., 2018). We interpreted the compositional and textural evidence to establish that the Copper Cliff member was formed by ballistic erosion and sedimentation processes (Oberbeck, 1975) as Endeavour ejecta impacted and mixed with rocks on the pre-Endeavour (locally Matijevic formation) surface (Mittlefehldt, Gellert, et al., 2018). Here we reexamine the possible connection between the Copper Cliff member and the Matijevic formation using our new AHCA results on a larger data set. Our previous AHCA modeling using a different linkage method and simple element/Si mole ratios, not log ratios. Use of the log ratios here makes the results more robust against the closure problem (Aitchison, 1994).

The compositional connection between the Copper Cliff member and the Matijevic formation is supported by our present modeling. In the first model, analyses of the Matijevic matrix (clastic rocks with few spherules) and two analyses of veneer on the Matijevic surface are in cluster 1 as are 63% of the Copper Cliff analyses (Table 4a). No other Shoemaker formation analyses are in cluster 1. The remainder of the Copper Cliff analyses are in cluster 2, along with the other analyses of the veneer. Two upper Shoemaker formation analyses are in cluster 2, anomalous rock Sledge Island1 and Parral. Parral is texturally like lower Shoemaker breccias from Perseverance Valley, such as Mesilla, and different from upper Shoemaker breccias, such as Waverly (Figure 9); it is plausibly lower Shoemaker. Analyses of the spherule-rich targets in the Matijevic formation are in cluster 9, part of major cluster B, and thus show no close compositional connection to the Copper Cliff member (or the other Matijevic formation targets for that matter). When the mobile elements P, Mn, Ni and Zn are excluded from the modeling, all matrix and spherule-rich Matijevic targets and three of five of the veneer targets are in clusters 1 and 2, as are 63% of the Copper Cliff member analyses, but only two of upper Shoemaker targets. The new AHCA modeling confirms the compositional connection between the Copper Cliff member and the underlying Matijevic formation, and we conclude that formation by ballistic erosion and sedimentation processes (Oberbeck, 1975) remains a good model for understanding it.

We labeled four analyses of two targets (York and Jean Baptiste Deschamps) separately for the purposes of AHCA modeling, and the results show that they are compositionally distinctive. The western end of Marathon Valley is mapped as containing Fe-Mg smectite based on analysis of multiple CRISM images of the region, with a (Fe,Mg)-OH 2.29 μm band depth comparable to those from Mawrth Vallis (Fox et al., 2016). This signal encompasses most of the western valley floor, including most of the lower-1 and lower-2 APXS targets. During operations, a lower-1 outcrop containing targets York and Jean Baptiste Deschamps was modeled to be a locus of the strongest smectite signal and these two targets are separated as representing a "smectite region" (Table 1). The analyses of these targets are clearly distinguishable from those of other lower-1 targets in the AHCA modeling (Table 4a). Three of the smectite region analyses are the sole members of cluster 9 in major cluster B with the other being a member of cluster 8 (Figure M04); all other analyses of lower-1 targets are in major cluster C (Table 4a). Thus, the smectite region analyses are separated from the other lower-1 analyses at the B-C separation at the third most dissimilar linkage (distance ~10.3, Figure 8a).
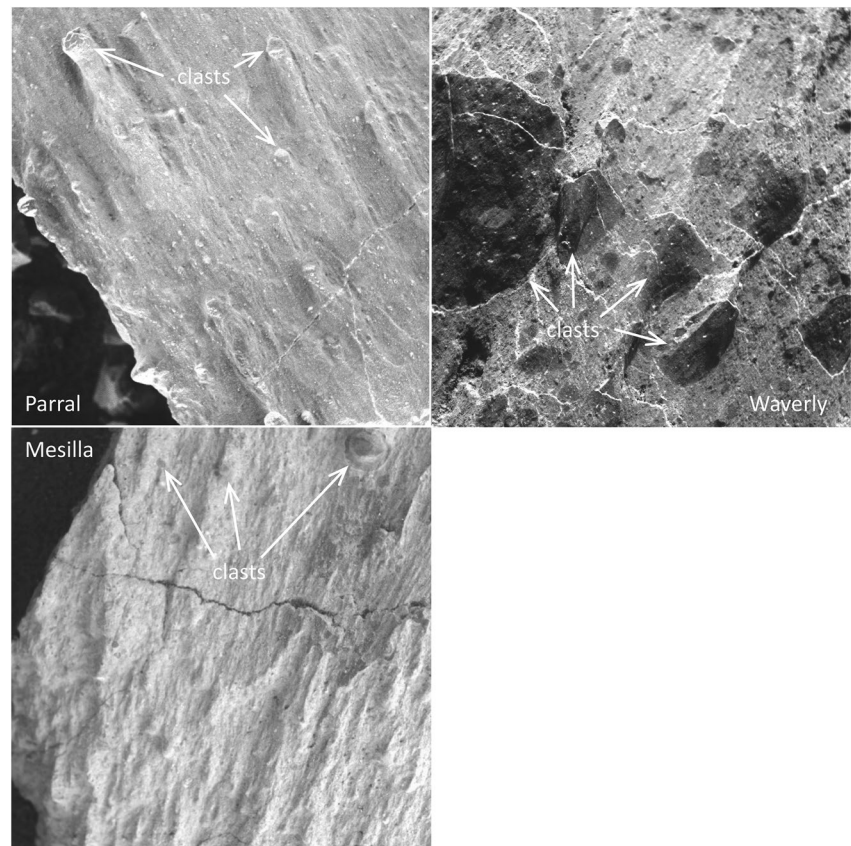
Figure 9. Individual Microscopic Imager (MI) frames of Parral (Sol 4809), Waverly (Sol 4656) and Mesilla (Sol 4900) documenting the distinct texture of Parral compared to the upper Shoemaker target Waverly but like that of lower Shoemaker Mesilla. Clasts in Waverly (dark) are more abundant and up to 18 mm in size, while those in Parral (heads of rock tails) are fewer and smaller (largest ∼3 mm across). Images are 31 mm across. The location of Parral and Mesilla can be found in Mittlefehldt et al. (2021), Figure L10; that of Waverly in Figure L08.

The smectite region rocks are less distinct from other lower-1 targets when the mobile elements are excluded from the AHCA modeling. In this case, the smectite region analyses still occur in a single cluster, but that cluster includes two other lower-1 analyses (Table 4b). Furthermore, 89% of lower-1 analyses are in major cluster II along with the smectite region analyses. This indicates that the smectite region rocks are not especially different in lithic components, but rather, their distinction is more closely tied to the alteration that engendered smectite formation.

4.3. Si-Rich Lithic Types and Pre-Endeavour Alteration

There are four silica-rich lithic types along Endeavour crater rim: (a) the Lihir/Espérance boxwork veins that crosscut the Matijevic formation on Cape York (Arvidson et al., 2014; Clark et al., 2016; Crumpler et al., 2015); (b) the red-zone group from the Marathon Valley region; (c) purple-rock erratic blocks first encountered on a ridge overlooking Marathon Valley; and (d) pitted rocks from Perseverance Valley. These four rock types share the common characteristic of having higher SiO_2 and lower FeO than Shoemaker or Matijevic formation rocks (Figure 6a), but for other elements, they can overlap the ranges for these formations and/or show distinct elemental trends between them (Figure 6). All the boxwork vein analyses are in major cluster B (Figure M04), while all purple- and pitted-rock targets are in major cluster D (Table 4a; Figure M08). The red-zone-group analyses are distributed amongst major clusters A (27%), B (9%) and D (64%) (Table 4a). When the mobile elements are excluded from the AHCA modeling, major cluster IV contains only silica-rich rocks, including all boxwork-vein, purple-rock and pitted-rock targets, and 82% of the red-zone-group targets (Table 4b).
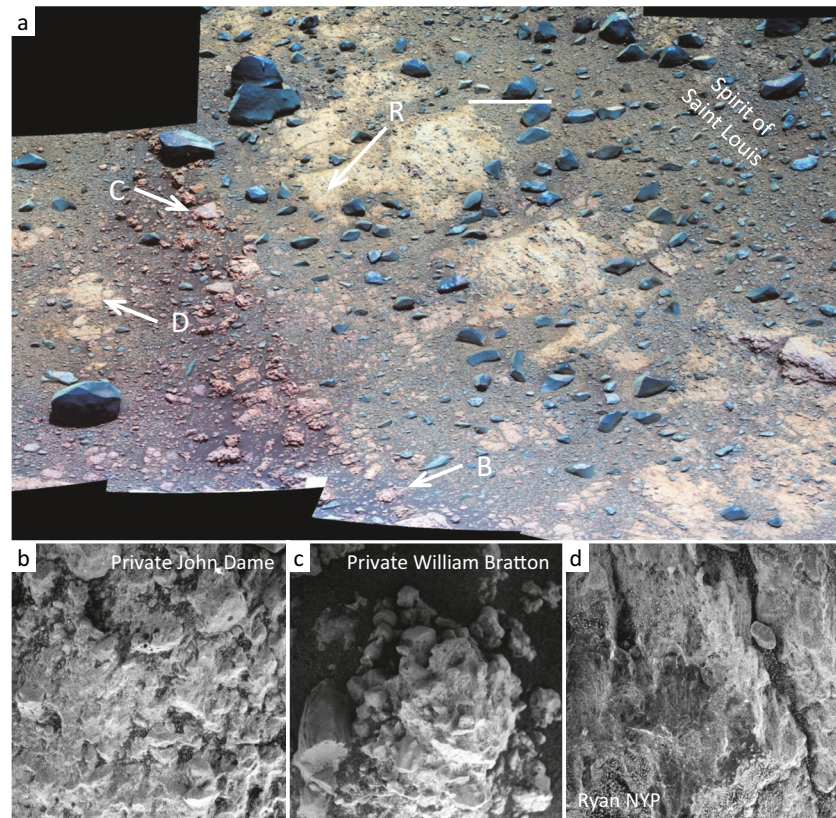
Figure 10. (a) Portion of a Pancam false-color mosaic (Sol 4033, L257) of red zone bordering north side of Spirit of Saint Louis with APXS/MI targets identified: (b) Private William Bratton; (c) Private Pierre Cruzatte; (d) Private John Dame; R–Ryan NYP. (b)–(d) Microscopic Imager (MI) images of three of the Alpha Particle X-ray Spectrometer (APXS) targets. Scale bar in (a) is ∼25 cm at the location shown. MI images are 31 mm across. The location of these images can be found in Mittlefehldt et al. (2021), Figure L05.

4.3.1. Boxwork Veins in the Matijevic Formation

The two abraded interiors of the boxwork veins have the highest SiO_2 and Al_2O_3 (Figure 6c), the lowest FeO, MgO, and CaO (Figures 6a, 6b, 6d) and show the cleanest compositional signal of the vein material (Clark et al., 2016). These two analyses have the highest SiO_2 and lowest FeO and CaO of any target analyzed on Meridiani Planum. The boxwork vein compositions are consistent with montmorillonite plus silica having been the dominant phases in the veins (Arvidson et al., 2014; Clark et al., 2016). These veins were formed from hydrothermal solutions that were circumneutral to mildly alkaline in pH (Clark et al., 2016; Mittlefehldt, Gellert, et al., 2018).

4.3.2. Red-Zone Group in Marathon Valley

Unique to the Marathon Valley region are prominent curvilinear features crosscutting outcrop blocks containing rock with distinctive reddish color in Pancam false-color images (Figure 10a) which we informally call "red zones" (Figure L06). At the head of Marathon Valley is a shallow, ovoid depression ∼25 × 35 m in size—Spirit of Saint Louis (Figure 1d)—which is partly bounded by a ∼10–20 cm wide band containing red-zone rocks crosscutting Shoemaker lower-2 outcrops. Some of the outcrop blocks near Spirit of Saint Louis also exhibit compositional similarities to the red zones. Red zones were found within Marathon Valley proper crosscutting both lower-1 and lower-2 subunits. After leaving Marathon Valley on a feature named Spirit Mound (Figure L08), we discovered an outcrop of lower-1 subunit bedrock cut by a composite silica-$CaSO_4$ vein-like structure which shows geochemical similarities to red-zone rocks. All these targets are referred to as the red-zone group. Red-zone features were not observed outside the region of Marathon Valley and immediate surroundings, nor in the upper Shoemaker subunit.

Excluding the vein on Spirit Mound, rocks in the cores of red zones consist of discontinuous cm-sized knobs of rock with a hackly, cemented appearance (Figure 10c). Many of them appear indurated, with clasts and matrix only poorly distinguished. They are distinct from rocks on either side of the red zone which are texturally typical of the Shoemaker lower-1 or lower-2 breccias which they crosscut (Figures 10b and 10d).

Red zone rocks have unique compositional characteristics (Figure 6). Most analyses occupy cluster 18 within major cluster D (Table 4a; Figure M08). The only other analyses in cluster 18 are two on lower-2 target Muffler II. The two red-zone analyses in cluster 3 are targets on Gasconade3 and 4, a red-zone-group vein on Spirit Mound. The other two outliers are Thermopylae2 and Private Pierre Cruzatte, which have higher Ni contents (as do Gasconade3 and 4) than the other red-zone-group analyses. When the mobile elements are removed from the AHCA analyses, Thermopylae2 and Private Pierre Cruzatte cluster with the other red-zone-group analyses, while Gasconade3 and 4 remain separated at the cluster level (Table 4b; Figure M15). Like the boxwork veins, the red-zone group has higher SiO_2 and lower FeO contents compared to Shoemaker formation breccias (Figure 6a). Furthermore, red-zone-group compositions follow the MgO–SiO_2 and CaO–SiO_2 trends of the boxwork veins (Figures 6b and 6d). One distinction between these two rock types is that the boxwork veins show strong enrichments in Al_2O_3, while the red-zone rocks show more modest enrichments, resulting in distinct Al_2O_3-SiO_2 trends (Figure 6c). The red-zone group has Al_2O_3, TiO_2 and Cr_2O_3 contents within ranges of Shoemaker lower-1 and lower-2 breccias (Figures 6c, 6e and 6f).

For the red zone around Spirit of Saint Louis we did three analyses each of red-zone rocks and the host rock on either side (Figure 10a). Compared to a weighted mean of these adjacent breccias (Ryan NYP, Ryan NYP2, Private John Dame), the red-zone rocks have enrichments in Al, Si, Ti, Cr and Ge (Figure 11a). Potassium contents are also higher than those of the nearby breccias but overlap the uncertainty envelope of the mean host rock. Phosphorus, Ca and Zn overlap the composition of the mean host rock, while the other elements are depleted relative to it. Considering only the red-zone target with the highest SiO_2 content, Private William Bratton (Figure 11a inset), Al, Si and Cr are well-resolved from the host rock, while the uncertainties on K and Ti overlap the uncertainty envelope on the host rock composition. Some bedrock blocks near the Spirit of Saint Louis feature have higher Al_2O_3 and SiO_2 contents indicating red-zone-style alteration extended beyond the narrow, visually defined red zones. Rocks on either side of the red zone and patches within it have Pancam spectra which more closely resemble that of red hematite, indicating the presence of crystalline ferric oxides within these rocks (Farrand et al., 2016).

Some rocks from the Spirit of Saint Louis region have Ge contents well above the detection limit of ~30 µg/g for long measurements in close contact. The highest Ge contents are observed for red-zone-group rocks (Table 5); Ge concentrations for Private William Bratton (853 µg/g) from the red zone proper, and Thermopylae2 (855 µg/g) from a nearby outcrop that has red-zone-group compositional characteristics, are the highest concentrations measured on Mars. For comparison, the Garden City vein cluster crosscutting Murray formation mudstones in Gale crater contains ~650 µg/g; the mudstones themselves are enriched in Ge to ~100 µg/g (Berger et al., 2017).

Germanium is mobilized in hydrothermal fluids, and hydrothermally altered seafloor basalts on Earth show modest enrichments of a few µg/g in Ge (e.g., Escoube et al., 2015). In terrestrial hydrothermal deposits, Ge substitutes in Fe-oxyhydroxides, sulfides or sulfosalts (Bernstein, 1985). There is no correlation between Ge and either Fe or S for the rocks around Spirit of Saint Louis, indicating that Fe-oxyhydroxides or S-bearing phases are not significant hosts for Ge. At Gale crater, measurements made by the Curiosity rover APXS instrument show that there is a broad positive correlation between Zn and Ge (Berger et al., 2017). In the Spirit of Saint Louis region Zn and Ge are anti-correlated, indicating a different mechanism for Ge enrichment than pertained at Gale crater.

Germanium concentrations in the region of Spirit of Saint Louis are roughly correlated with Al_2O_3 and SiO_2 (Figure 11b). Tetravalent Ge and Si have similar chemical properties, and Ge substitutes for Si in minerals (e.g., see He et al., 2019). Hence, Ge is most likely substituted in the silica phase in the red zones. The highest Ge content in red-zone target Private William Bratton is well above the values of the nearby Shoemaker lower-2 host rocks (Figure 11b; Table 5) and such levels of enrichment cannot have resulted from passive concentration as more soluble elements were leached away; Ge must have precipitated from solutions. This in turn suggests that a portion of the silica is a precipitate. Alumina, Ti and Cr are also concentrated in the
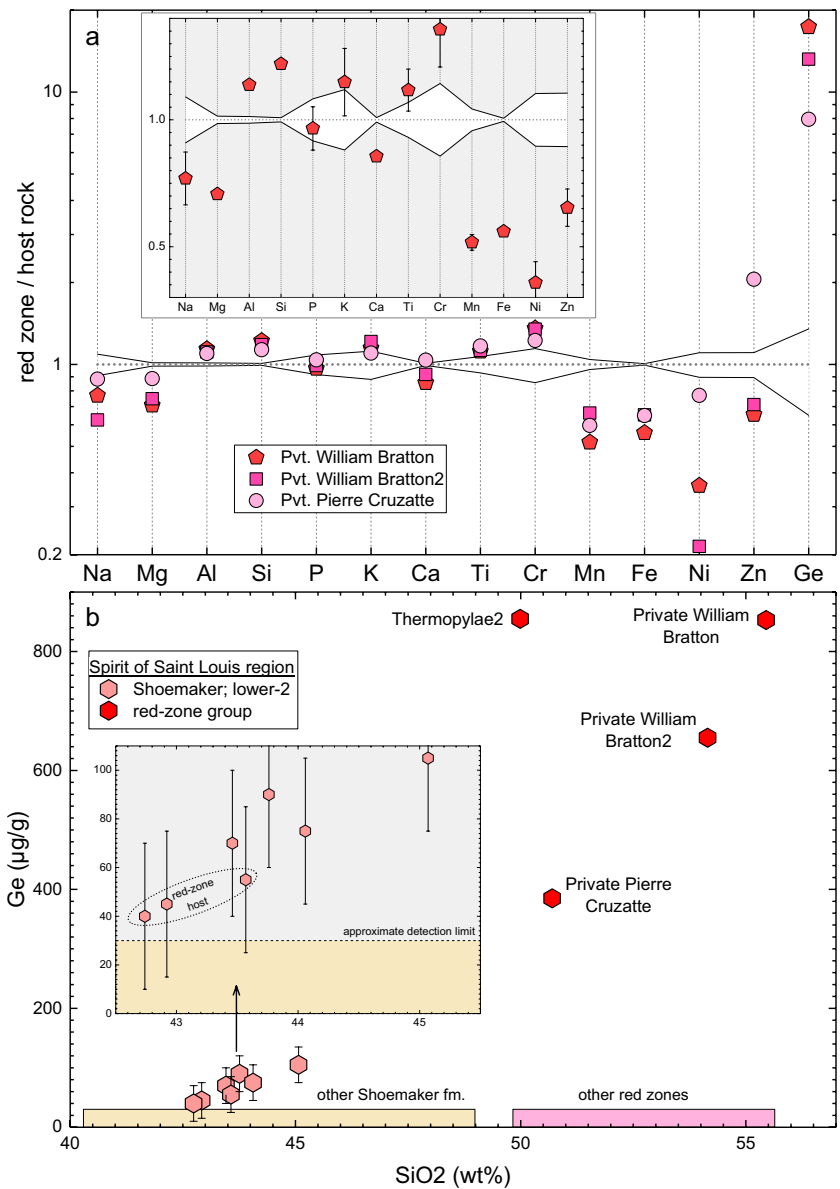
Figure 11. Element enrichments and depletions of red-zone rocks. (a) Comparison of red zone on the border of Spirit of Saint Louis with average host bedrock on either side; inset shows details for enriched elements in Private William Bratton target. Ratio uncertainties are shown when larger than the symbol size. (b) Ge versus SiO_2 for rocks around Spirit of Saint Louis compared to similar rocks from Marathon Valley; inset expands the view of lower-2 Shoemaker rocks, with the three host rocks used for normalization of red-zone rocks in (a) encircled. Boxes on abscissa represent approximate detection limits for Ge, which encompass most analyses from Marathon Valley.

red-zone rocks, and these elements can be conserved during hydrothermal alteration. A possible scenario for the red-zone-group rocks in the vicinity of Spirit of Saint Louis is fluxing of hydrothermal fluids through fractures and nearby porous bedrock in the region which resulted in localized alteration and leaching of the more soluble elements at high water/rock, followed by precipitation of Ge-bearing silica. Hydrothermal solutions in equilibrium with Ge-bearing silicates have higher Si and Ge concentrations and Ge/Si ratios at higher temperatures (Pokrovski & Schott, 1998). Thus, simple cooling of solutions during waning stages of hydrothermal activity could result in precipitation of Ge-rich silica.

The rocks in the Spirit of Saint Louis region show enrichments in Ge, but other bedrock and red-zone-group targets from the Marathon Valley region do not have detectable Ge (detection limit roughly 30 µg/g,

but dependent on target composition and analytical conditions) (Figure 11b). This might suggest that there were differences in fluid compositions and/or properties (temperature, pH, etc.) at this location. However, red-zone rocks with identical enrichments in Al_2O_3 and SiO_2 and depletions in FeO have vastly different Ge contents (Figure 11b). Any differences in fluid compositions and/or properties would have to be such that the major elements were not affected. For example, fluid composition could have been affected by earlier mineral precipitation, and in terrestrial systems, the Ge/Si of fluids can be increased by this process (Escoube et al., 2015; Mortlock et al., 1993). This is unlikely to explain high- and low-Ge red-zone rocks with similar SiO_2 contents as early precipitation of silica is commonly invoked to explain such fluids (Escoube et al., 2015; Mortlock et al., 1993). An alternative hypothesis is that the bedrock below Spirit of Saint Louis is atypically rich in Ge, but this merely pushes the cause of Ge enrichment beyond our ability to test.

4.3.3. Purple Rocks in the Marathon Valley Region

Purple rocks are erratic boulders scattered on a ridge overlooking the northeast side of Marathon Valley and on the valley floor at the base of the ridge (Figure L18). They are identified by unique purplish color in Pancam false-color composites (753, 535, and 432 nm) and a fine-grained, almost aphanitic texture. The five analyses of this lithic type represent three different rocks. Their silica contents are only marginally greater than those of Shoemaker formation breccias, but their Al_2O_3 contents are much higher (Figure 6c); two analyses of target Sergeant Nathaniel Pryor are the highest Al_2O_3 contents measured on Meridiani Planum. Compared to the boxwork veins and red-zone group, the purple rocks have very low MgO and Cr_2O_3, Ni below the detection limit, and widely varying TiO_2 (Table 1, Figures 6b, 6e and 6f). These elemental distributions are very different from the alteration signatures exhibited by the boxwork veins and red-zone group.

The silica- and alumina-rich compositions of the purple rocks could represent evolved igneous compositions, but the case is not clear. On a total alkalis-silica diagram often used to classify martian igneous rocks (e.g., McSween et al., 2006; Sautter et al., 2015), they fall in the field of basaltic andesite. Igneous fractionation from basaltic to intermediate compositions show generally increasing Al_2O_3 with SiO_2, and decreasing MgO, CaO, Cr_2O_3 and Ni (for example, the tholeiite to icelandite series at the Torfajökull volcanic complex, Macdonald et al., 1990). Dark-rock boulder-float and rocks from Wdowiak Ridge are potential pre-Endeavour basaltic rocks (Mittlefehldt, Gellert, et al., 2018), and the blue rocks are basaltic in composition. Elemental trends between these rock types and the purple rocks (Figure 6) are consistent with an igneous fractionation sequence. However, the wide range in TiO_2 contents with little change in MgO or Cr_2O_3 is inconsistent with simple igneous fractionation; a strong anticorrelation would be expected.

4.3.4. Pitted Rocks in Perseverance Valley

We encountered deeply pitted rocks in a linear outcrop in the central portion of Perseverance Valley (Figure L21); these pitted rocks are thought to occupy a fracture zone, possibly a fault trace, within the valley (Crumpler et al., 2020). They have a fine-grained granular texture, lack visible clasts, and contain mm-sized pits of uncertain origin (Tait et al., 2019). Dark, fine-grained granular material is present within some pits which appears to be dark sand, but some pits contain orangish-red (in false color) fine-grained fillings texturally reminiscent of zeolites filling vesicles in altered basalt (Figure 13). These fillings have deep 535 nm absorption bands indicative of abundant nanophase ferric oxides. Other pits have bright rims; bright coatings or rinds on parts of some pitted rocks give spectral evidence of alteration (Farrand et al., 2019; Tait et al., 2019).

The five analyses of pitted rocks represent two different rocks and show varied compositions. The three analyses with the lowest SiO_2 (targets Allende and Nazas) are in cluster 19 along with the purple rocks (Table 4a). The other pitted rock analyses (target Tomé) are in cluster 20. Target Nazas was centered on a pit filled with fine-grained, acicular crystals to capture the composition of alteration material and yielded a silica content intermediate between Allende and Tomé. The Tomé analyses have the highest SiO_2 contents of any target from Marathon and Perseverance Valleys and rival the highest SiO_2 contents measured for the boxwork veins in the Matijevic formation (Figure 6). Unlike the boxwork veins, the pitted rocks do not show a positive correlation between Al_2O_3 and SiO_2 (Figure 6c).

The similarity between Allende and the purple rocks suggest that this pitted rock could be an evolved magmatic composition. The low MgO, FeO and Cr_2O_3 contents (Figures 6a, 6b and 6f) and Ni below detection all support this. However, the morphology and location of the pitted rocks as a linear feature in a probable
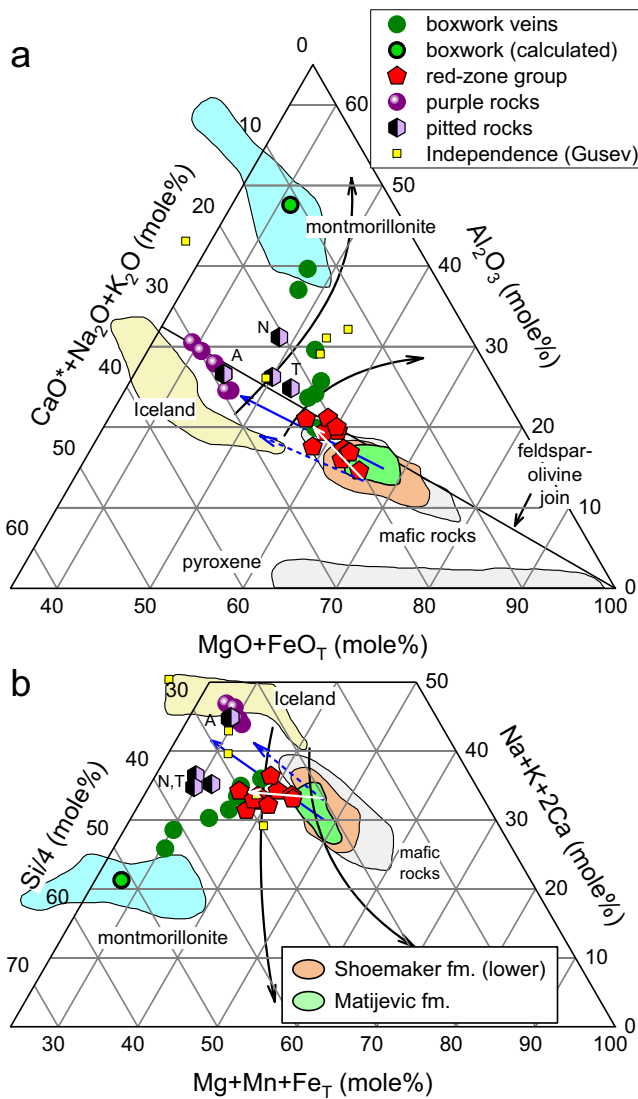
Figure 12. Alteration diagrams for Endeavour crater rim rock types, after (a) Nesbitt and Wilson (1992) and (b) Meunier et al. (2013). Blue arrows show expected change for alteration under low water/rock in which olivine dissolves (Hurowitz & McLennan, 2007). White arrow joins host bedrock with red-zone rock from Spirit of Saint Louis (see Figure 10). Curved arrows show alteration changes in Monaro basalts (Eggleton et al., 1987). Labeled pitted rock symbols are: (a) Allende; N–Nazas; T–Tomé. Independence-class rocks from Gusev crater shown for comparison. See text for definition of CaO*.

fault trace are not that of volcanic unit. The formation mechanism for these rocks is uncertain (see Tait et al., 2019). They could be pseudotachylite formed in the fracture either by impact or tectonic processes (Reimold, 1995). Pseudotachylite is a cataclastic rock but the pitted rocks to not appear to be. The pitted rocks are juxtaposed with dark basaltic rock in the fracture zone (Crumpler et al., 2020) and clasts of dark basalt in the dark-melt matrix might have been difficult to distinguish in the rover images. The silica-rich Tomé targets cannot be more evolved magmatic compositions than Allende because there is no substantial depletion in them of MgO, FeO, and Cr_2O_3 compared to Allende. An alternative hypothesis is that Tomé is an altered composition of rock that might initially have been like Allende.

4.3.5. Evaluation of Alteration in Si-Rich Rocks

Chemical alteration diagrams are used to document compositional changes in terrestrial rocks caused by alteration and weathering. Figure 12a is a portion of an Al_2O_3, (CaO*+Na_2O + K_2O), and (FeO_T+MgO) (A-CNK-FM) diagram (Nesbitt & Wilson, 1992), and Figure 12b is a portion of a modified weathering intensity scale (WIS) diagram (Meunier et al., 2013). These diagrams were devised to evaluate compositional changes occurring in rock during soil formation. In the A-CNK-FM diagram, CaO* is measured CaO minus that contained in apatite and carbonate (Nesbitt & Wilson, 1992). We assumed all P_2O_5 is in apatite and ignored calcite because CO_2 is not determined by the APXS. Furthermore, we did not correct CaO (or any other species) for SO_4 or Cl; effectively, we treated these anions as having been added as acidic components. In the modified WIS diagram we treat all iron as FeO because we have no measure of the ferric/ferrous ratio for the rocks. In Figure 12a, pristine basaltic to intermediate igneous rocks will plot between the feldspar-olivine join and the field for pyroxenes, as is observed for martian mafic rocks (blue rocks from the Endeavour crater rim, and Adirondack-, Backstay- and Algonquin-class rocks from Gusev crater) (cf., Figure 9 of McGlynn et al., 2012). On both diagrams, magmatic differentiation will cause rock compositions to move from the field for mafic rocks in the general direction toward the purple rocks. This is illustrated by a suite of tholeiites through icelandites from the Torfajökull volcanic complex (Macdonald et al., 1990). Low-temperature alteration on Earth (pedogenesis) of a range of primary rocks drives compositions into the Al_2O_3 side of Figure 12a (Nesbitt & Wilson, 1992) and away from the Na+K+2Ca apex of Figure 12b (Meunier et al., 2013), as illustrated by altered Monaro basalts from New South Wales, Australia (curved arrows) (Eggleton et al., 1987). On Mars, alteration under low water/rock, acidic conditions in which olivine is preferentially dissolved with the R^{2+} cations leached away would change pristine martian basalt compositions directly away from the MgO+FeO_T (+MnO) apexes (blue arrows) (Hurowitz & McLennan, 2007). Note that hydrodynamic sorting of soils could also change compositions following the blue arrow (Fedo et al., 2015; McGlynn et al., 2012). A fine-grained clastic sedimentary rock could give the appearance of having been altered when only density sorting during transport of unaltered clastic particles occurred.

The four silica-rich rock types from the Endeavour crater rim show differing trends on the alteration diagrams resulting in differing interpretations. The clearest signature for alteration is shown by the boxwork veins crosscutting the Matijevic formation. Compositions of the two abraded targets fall near or within the field of terrestrial montmorillonites (Figure 12) (Wolters et al., 2009), consistent with the interpretation of Clark et al. (2016). Clark et al. (2016) calculated a pure vein composition for the Espérance vein analyses by correct-
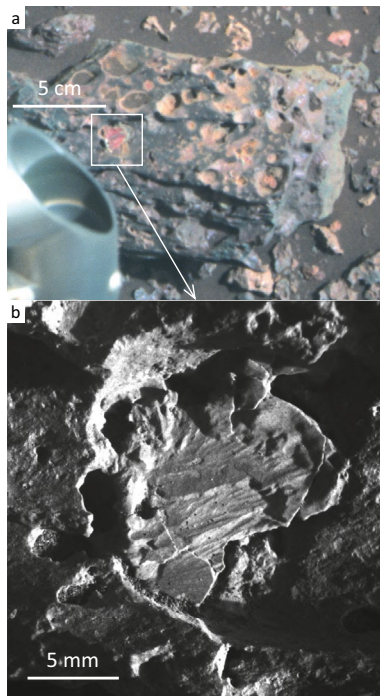
Figure 13. Images of pitted Nazas target from Perseverance Valley. (a) Portion of Pancam false-color image (Sol 5042, L257) highlighting pit filled with reddish-orange alteration material. (b) Portion of Microscopic Imager image (Sol 5053) of the pit showing texture of the alteration material. The location of (a) can be found in Mittlefehldt et al. (2021), Figure L09.

ing the instrument response for a small amount of veneer material that was in the APXS field of view. The resulting composition plots well within the fields for montmorillonite (Figure 12). Five analyses by sister rover Spirit of rock Independence from Gusev crater are shown for comparison as this rock is thought to contain an alteration component close in composition to montmorillonite (Clark et al., 2007). The rock shows clear evidence for alteration, but the signature for montmorillonite is not as clearly expressed as for the boxwork veins. The red-zone group shows less dramatic evidence for alteration on these diagrams, however, tie lines joining the host rock composition for Private William Bratton with that red-zone target (white arrows) diverge from vectors expected for alteration under low water/rock, acidic conditions (blue dashed arrows). This, plus the arguments given in Section 4.3.2 for coprecipitation of Si and Ge, indicates that compositions of red-zone-group rocks are not derived by simple passive enrichment as ferromagnesian cations released by olivine dissolution are leached away.

The purple rocks show conflicting evidence regarding whether they are altered compositions and if so, how they might have been altered. These rocks have compositions broadly consistent with their being intermediate melts from a basalt fractionation sequence, especially the two analyses of Bashful II which have the lowest Al_2O_3 contents (Figure 6c). The two purple rock analyses with highest Al_2O_3 (Sergeant Nathaniel Pryor) have CIPW norms that are marginally corundum normative (one is, one is not). Corundum-normative compositions indicate rock compositions that have been significantly altered from those of pristine magmatic rocks (cf., Ming et al., 2006; Mittlefehldt, Gellert, et al., 2019). The texture of purple rocks is consistent with a fine-grained, quenched melt. The evidence suggests the purple rocks are slightly altered intermediate magmatic rocks. They could be fragments of impact melt of slightly altered target rock with a mixed composition like that of intermediate magmatic rocks, but they do not contain observable clasts in Pancam or MI imagery.

Macroscopic and microscopic clasts commonly occur in impact melts, but their lack in purple rocks does not preclude an impact-melt origin for them. Observations of flow features in some impact-melt deposits in lunar craters indicate relatively fluid flow for extended periods after the impact event (Bray et al., 2010). The morphology of some impact-melt deposits indicates low viscosities, and therefore, low clast contents (Bray et al., 2010; Stopar et al., 2014). Thus, an origin as fragments of an old ponded impact-melt sheet remains viable for the purple rocks.

The pitted rock Allende mimics the purple rocks on the alteration diagrams, while the Nazas and two Tomé targets show clear evidence of the effects of alteration. The Allende analyses are fully consistent with a pristine intermediate magmatic composition. It is not corundum normative, and, ignoring the ubiquitous SO_3, Cl, and Br, shows no compositional evidence for alteration. As is the case for the purple rocks, an impact melt origin is viable, specifically as pseudotachylite. The Nazas analysis was targeted on a pit largely filled with reddish orange (in false color) acicular alteration material (Figure 13), and its composition has excess Al and a deficit in Na+K+-2Ca compared to the Bashful II analyses. These characteristics and the texture are consistent with formation as a pit filling formed through alteration under relatively high water/rock. Tomé is marginally on the Al-rich side of the feldspar-olivine join in Figure 12a and plots with Nazas on Figure 12b, indicating an altered composition, consistent with Pancam spectral evidence (Farrand et al., 2019; Tait et al., 2019).

4.4. Sulphate-Rich Rocks and Post-Endeavour Alteration

We have previously documented episodes of sulfate-dominated alteration at several locations along the Endeavour crater rim hosted in the Matijevic, upper Shoemaker and Grasberg formations (Arvidson et al., 2014, 2016; Crumpler et al., 2015; Mittlefehldt, Gellert, et al., 2018; Squyres et al., 2012). Except for alteration in the Cook Haven region (Arvidson et al., 2016), the sulfates are dominantly $CaSO_4$ in crosscutting
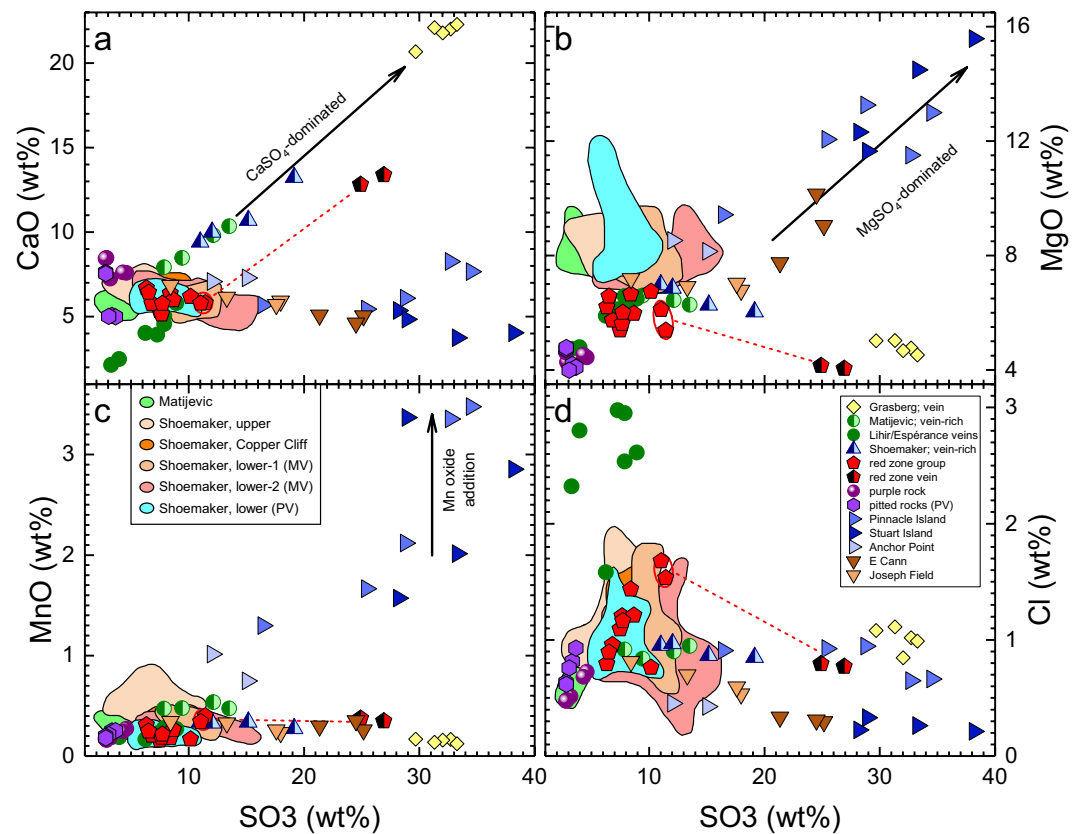
Figure 14. Element versus SO_3 diagrams for altered rocks and soils from the Endeavour crater rim. Red circles enclose Si-rich red-zone-group targets from Gasconade, which also includes $CaSO_4$-rich components (red dashed tie lines).

veins (Figure 14a). Coarse $CaSO_4$ veins occur in upper Shoemaker outcrops on Cape Tribulation (Mittlefehldt, Gellert, et al., 2018) and in the Grasberg formation which drapes over the lower reaches of the upper Shoemaker (Crumpler et al., 2015; Squyres et al., 2012). These observations document a period of $CaSO_4$ precipitation from dilute solutions after formation of Endeavour crater and likely after deposition of at least a portion of the Burns formation of sulfate-rich sandstones (Mittlefehldt, Gellert, et al., 2018). Thin $CaSO_4$ veins crosscutting the Matijevic formation (Arvidson et al., 2014) represent an earlier, pre-Endeavour-impact period of sulfate precipitation, based on superposition relationships; they are truncated by alteration veneers that were formed on an unconformity surface between the Matijevic and Shoemaker formations (Mittlefehldt, Gellert, et al., 2018).

In the Cook Haven region (Figures 1c, and L15), sulfates were found as coatings on rock fragments overturned by Opportunity's wheels; these are dominated by Mg-sulfates (Arvidson et al., 2016). Cook Haven lies in a gentle depression on Murray Ridge where highly fractured outcrops are exposed; the region is thought to be within a fracture zone transecting the rim (Arvidson et al., 2016). The rock coatings on Pinnacle Island and Stuart Island and the disturbed soil Anchor Point show positive correlations between Mg and S, but not Ca and S (Figures 14a and 14b). These rock coatings include the highest measured SO_3 contents on Meridiani Planum. They are also rich in MnO (Figure 14c); Pinnacle and Stuart Islands have the highest MnO contents measured on Meridiani Planum and Ni is positively correlated with MnO (Arvidson et al., 2016). The high Mn contents are identified from Pancam 13-filter spectra as arising from one or more Mn oxides (Arvidson et al., 2016). Further, the rock coatings on Pinnacle Island have high P_2O_5 contents; the second and third highest on Meridiani Planum (Arvidson et al., 2016). The compositions and mineralogies of the coatings reflect precipitation of phases from solutions formed through alteration of basaltic composition protoliths (Arvidson et al., 2016).
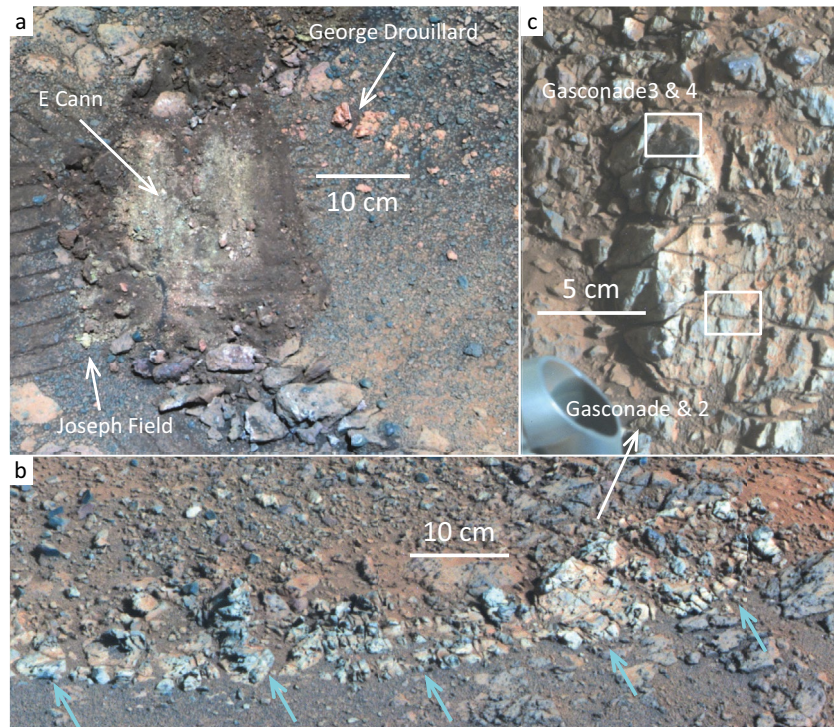
Figure 15. (a) Pancam false-color image (Sol 4404, L257) of the wheel scuff exposing altered soils in a fracture in Shoemaker lower-1 showing locations of Alpha Particle X-ray Spectrometer (APXS) targets. The line of red pebbles is a red zone transecting the outcrop. (b) Pancam false-color image (Sol 4504, L257) of the Gasconade vein complex (cyan arrows) cross cutting Shoemaker lower-1 on Spirit Mound; region of (c) indicated. (c) Pancam false-color image (Sol 4505, L257) of a portion of the Gasconade vein complex showing locations of APXS targets; $CaSO_4$-rich Gasconade and Gasconade 2, and Si-rich Gasconade3 and Gasconade 4. The location of (a) can be found in Mittlefehldt et al. (2021), Figure L07; that of (b and c) in Figure L08.

A S-rich region associated with fractures through Shoemaker lower-1 bedrock was found in Marathon Valley (Figure 15a). The bedrock includes a red-zone-group vein adjacent to the S-rich region. Regolith in the fractures shows some compositional similarities to the altered rocks and soils at Cook Haven. The two soil targets E Cann and Joseph Field show a positive correlation between Mg and S, but not between Ca and S (Figures 14a and 14b), but unlike the Cook Haven rock coatings, E Cann and Joseph Field do not show elevated MnO (Figure 14c) or P_2O_5. The high MnO content of rock coatings on Pinnacle and Stuart Islands is considered to have been caused by late oxidation of solutions prompting precipitation of Mn oxides (Arvidson et al., 2016). The compositional signature of E Cann and Joseph Field is consistent with a similar formation mechanism as that of the Cook Haven rock coating, minus the oxidation/precipitation of Mn oxides and P enrichment.

The similar colored targets in the vicinity of E Cann and Joseph Field had Pancam 13f spectra with a shallow absorption band centered between 803 and 864 nm (the Pancam R3 and R4 bands). This absorption was comparable, albeit weaker in depth, and with a steeper blue to red slope and concomitant diminishment of reflectance in the 673 nm (L3) band, as those observed in spectra associated with light-toned, disturbed, sulfur-rich soils observed by the Spirit rover in the Columbia Hills of Gusev crater (Figure 16) (Farrand et al., 2016; Johnson et al., 2007).

Opportunity traveled eastward after leaving Marathon Valley toward the interior of Endeavour crater to investigate the small knob Spirit Mound (Figure L08) which we thought might expose Matijevic formation outcrops. Mapping showed that bedrock at Spirit Mound was Shoemaker lower-1 (Crumpler et al., 2020) that included a bright-vein-complex named Gasconade (Figure 15b). We did two APXS measurements each of the vein interior and edge (Figure 15c). The edge samples, Gasconade3 and Gasconade4, clustered with the red-zone group in our early AHCA modeling and we include them with this group here. However,
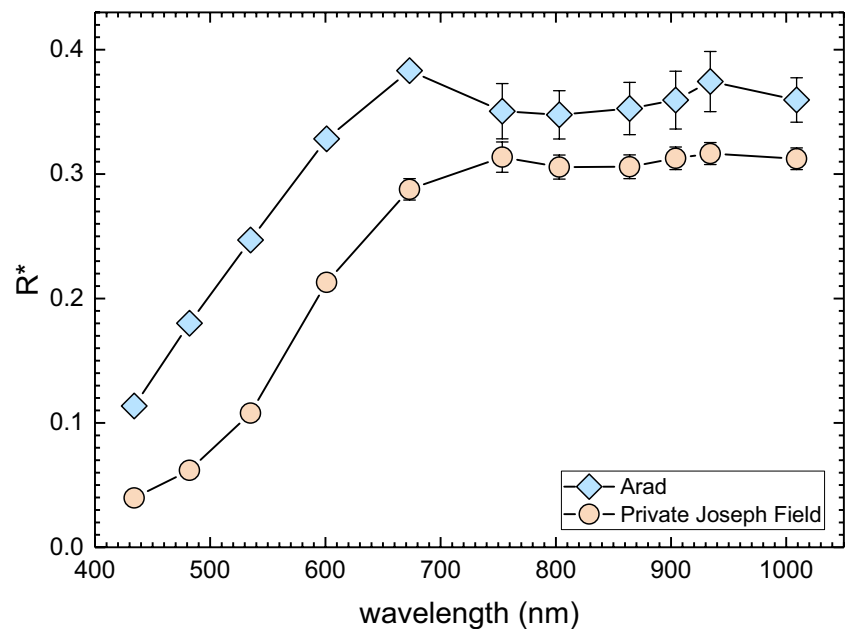
Figure 16. Comparison of Pancam spectra from light-toned soil exposed by Spirit rover scuff at the Arad target (MER-A Sol 721) and the yellow pebble Private Joseph Field at Opportunity's E Cann scuff area (MER-B Sol 4379) (Figure 15a). Each has a broad absorption centered between 803 and 864 nm attributed to Fe sulfate mineral(s). R* is relative reflectance; standard deviations are shown when larger than the symbol size.

although these targets are Si-rich like the red-zone group, they are Al-poor compared to that group (Figure 6c). The limited data on hand do not allow us to determine the mechanism of SiO_2 enrichment. Because the Si-rich sample is hosted in pre-Endeavour bedrock and has compositional signatures like those of other pre-Endeavour altered rocks, we interpret this as a pre-Endeavour alteration. The interior samples are sulfate-rich, and tie lines between the silica-rich and sulfate-rich samples indicate $CaSO_4$ dominates (Figure 14a and 14b). As discussed above, $CaSO_4$ veins are common in post-Endeavour rocks suggesting that Gasconade and 2 might have been precipitated much later from solutions following an older vein system. However, pre-Endeavour $CaSO_4$ veins are also present in the Matijevic formation. Thus, the timing of formation of the Gasconade $CaSO_4$ veins relative to the Endeavour impact is indeterminant.

The results of compositional measurements of alteration materials along the crater rim demonstrate that alteration in the pre-Endeavour basement commonly resulted in precipitation of silica $\pm$ alumina with some $CaSO_4$ precipitation, and that this reflects alteration by circumneutral solutions (Clark et al., 2016). In contrast, post-Endeavour alteration was dominantly a sulfate-forming process. We suggest that the Mg-sulfate alteration observed at Cook Haven and Marathon Valley likely was a response to hydrothermal solutions flowing through fractures in the bedrock closely associated in time with the impact event. The crosscutting $CaSO_4$ veins in upper Shoemaker and Grasberg formations represent a much later episode of sulfate precipitation that occurred after Burns formation sulfate-sands were being deposited at Meridiani Planum (Mittlefehldt, Gellert, et al., 2018).

4.5. Surface Versus Interior Composition

We have investigated five Shoemaker formation targets where we analyzed untreated, brushed and abraded targets to get information on compositions of the interiors, possible coatings, and the differences between them to evaluate possible surface-alteration zones: Private Robert Frazer; Pierre Pinaut; Private John Potts; Aguas Calientes; and Salisbury. Private Robert Frazer is from an outcrop situated on the northern side of Marathon Valley, east of a short ridge that forms part of the northern wall of the valley, while Pierre Pinaut is from an outcrop near the southern margin of Marathon Valley, approximately 50 m southwest of Private Robert Frazer (Figure L06). These targets are on outcrops of Shoemaker lower-1. Private John Potts
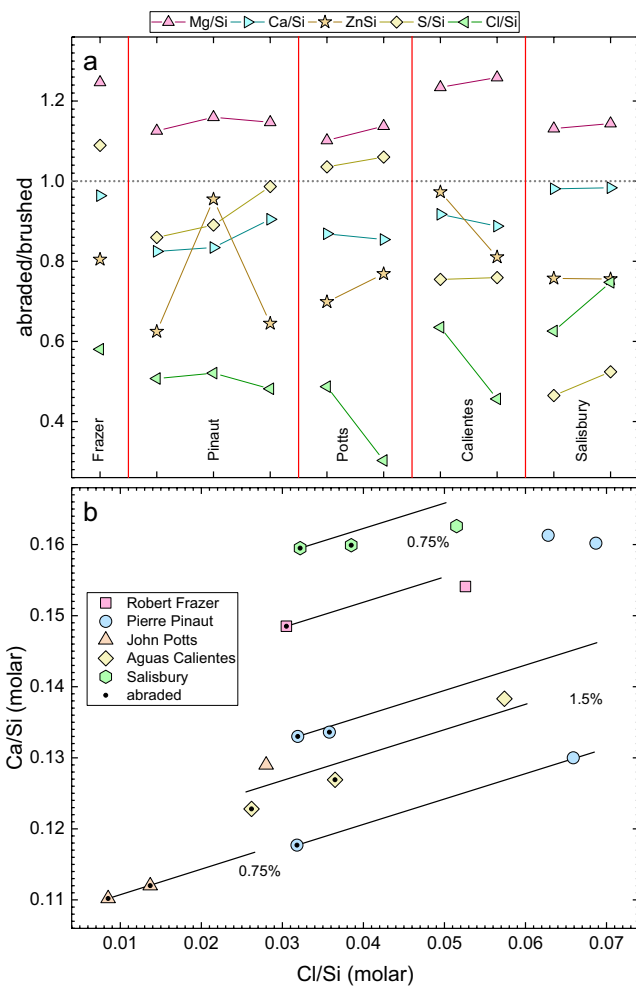
Figure 17. (a) Molar element/Si in abraded interiors normalized to brushed surfaces for select elements. (b) Molar Cl/Si versus Ca/Si for abraded and brushed targets, with the effect of adding 0.75 or 1.5 wt% $CaCl_2$ to interior compositions shown (see text).

is from a Shoemaker lower-2 outcrop located along the southern margin of Marathon Valley near Opportunity's egress point from the valley. It is about 60 m due east of Private Robert Frazer and ~90 m northeast of Pierre Pinaut (Figure L06). Aguas Calientes is from a lower Shoemaker outcrop block situated in the middle of Perseverance Valley roughly at the furthest point into the valley explored by Opportunity (Figure L10). Salisbury is from the Chester Lake member of the Shoemaker formation located on the southeastern end of Cape York. This outcrop was discussed by Squyres et al. (2012) where it was referred to as Chester Lake.

We normalized interior compositions to the cleanest brushed surface compositions for each target, and to the extent possible, compare brushed with interior compositions taken at identical APXS coordinates. Two abrasion activities were done on each of the rocks. We discuss the results for each abrasion for Private John Potts, Aguas Calientes and Salisbury. For Private Robert Frazer, the initial grind resulted in a partial abrasion circle, and APXS analyses on the brushed surface were not co-located with the post-abrasion spot. The analysis after the initial abrasion is not discussed. For Pierre Pinaut, the first grinding operation on did not significantly abrade the surface. The APXS results after the first abrasion were considered the cleanest surface analysis and used for normalizations for this target. The analysis campaigns resulted in eight interior-exterior pairs for the various lower Shoemaker targets, and two for Salisbury.

A qualitative synopsis of the interior/exterior results is given in Table 6 where a 3σ uncertainty level is used to identify elements in interior compositions that are greater than, less than, or equal to the brushed surface analyses. Silica is the most abundant element in Shoemaker formation breccias, and variations in Si within the suite are relatively small. At the 3σ level, Si mass-ratios are greater in the interiors than the exteriors in about half the targets, and equal to them in the other half. The closure restraint on major element analyses can cause false correlations (Chayes, 1971); to avoid false conclusions, we have evaluated only Si-normalized mole-ratios.

Quantitative comparisons of interiors to exteriors using Si-normalized mole-ratios (hereafter, ratios) show several commonalities among the lower Shoemaker breccias (Figure 17a). Magnesium ratios are greater in all 10 interiors, while Ca and Cl are lower in all, demonstrating unambiguous evidence for systematic compositional differences between interiors and cleaned surfaces. Sulfur ratios are lower in the Pierre Pinaut and Aguas Calientes targets except for one of the three Pierre Pinaut targets where it is slightly lower but within 3σ of the brushed analysis. Sulfur ratios are higher in Robert Frazer and Private John Potts interiors. The Br ratios (not shown) of Private Robert Frazier and Aguas Calientes are higher in the interiors, but for Pierre Pinaut and Private John Potts the interior and brushed targets are equivalent within uncertainty. If we relax the confidence level to 2σ, Zn ratios are lower in the interiors of seven targets and are never higher in the interiors.

The common depletions in Ca and Cl in the interiors relative to brushed surfaces suggests that these elements were mobilized out of the shallow interiors and onto surfaces. In general, addition of Ca and Cl in a mole ratio of 1:2 to interior compositions can replicate the Ca/Si and Cl/Si ratios of the brushed surfaces (Figure 17b). Only small amounts of Ca-Cl salt would need to be added; roughly 0.75–1.5 wt% if the salt is $CaCl_2$, more if it is a perchlorate. The Private John Potts and two of the Pierre Pinaut brushed surfaces have excess Ca over the simple model of Ca-Cl-salt addition. Unfortunately, there is no definitive explanation for these three brushed surface compositions, although mobilization of additional Ca salts could be the cause. The interior/exterior differences support a scenario in which Ca salts, dominated by Cl-bearing salts, have been wicked to the surfaces of rocks by small amounts of water.

The cause for higher Mg ratios in interiors is difficult to explain because there is no measured anion that could suggest mobilization of specific Mg salts in all cases. The abraded targets of Private Robert Frazer and Private John Potts have coupled enrichments of Mg and S, and removal of $MgSO_4$ from the surface targets (or deposition in the interior) could explain the higher MgO contents of the interior targets. For the other target. all measured anions excluding Br are lower in the interiors, but Br is at too low a concentration to balance variations in Mg content. This implies that the anion in a Mg salt is a light element not detected by the APXS, with carbonate being a plausible candidate. Magnesium carbonate is detected elsewhere on Mars and is especially prevalent in Nili Fossae where it is associated with olivine-rich units (e.g., Ehlmann et al., 2008; Niles et al., 2013). Magnesium-rich carbonate formation occurs during alteration of olivine to serpentine (e.g., Brown et al., 2010; Viviano et al., 2013). Magnesium-rich carbonate was detected by sister rover Spirit in Gusev crater as an alteration phase in the Comanche Spur outcrop, but this carbonate was calculated to contain a significant siderite component (Morris et al., 2010). There is no systematic difference for Fe between interior and surface analyses and thus any carbonate deposited in the interiors does not contain a significant siderite component.

The increase in Mg/Si in the interiors implies differential mobility of Mg relative to Si but the mechanism cannot be uniquely determined. The increase in Mg/Si could indicate either loss of Si from the surface or deposition of Mg just below the surface, but the latter is more plausible. A possible scenario to explain the common Mg, Ca and Cl differences between surfaces and ~1 mm depth in the Shoemaker breccias is as follows:

1. Thin films of water periodically form on rock surfaces when atmospheric conditions allow, which penetrate the interior by capillary action.
2. Soluble alteration products within the rock are taken into solution.
3. As water evaporates from the surface, the least soluble salts precipitate in voids in the rock, gradually filling cracks.
4. The most soluble salts, such as $CaCl_2$ or $Ca(ClO_4)_2$, are concentrated on the surface as the last of the water evaporates.

The occurrence of a similar interior/surface compositional pattern for Shoemaker formation breccias from Cape York, Marathon Valley and Perseverance Valley demonstrates that it is a regional process that likely is relatively young. Rocks in Marathon and Perseverance Valleys show "rock tails"—small aligned linear ridges of matrix material emanating from clasts standing above the general outcrop surface—which are interpreted as abrasion shadows formed as saltating sand planes down outcrop surfaces (e.g., Sullivan et al., 2005). The rock tails are often several mm in width and of comparable height (Figure 9). The amount of surface removed from the outcrop is thus at least of the same order as the typical depth of abrasion (1–2 mm) and indicates that formation of the Ca-Cl-rich crust is keeping pace with the abrasive removal of the outcrop surface. Golombek et al. (2006) have estimated denudation rates on Meridiani Planum during the Amazonian to be 10^{-2} to 10^{-3} m/Myr. If this rate applies to Marathon and Perseverance Valleys, then only 200,000 to 2,000,000 years is required to strip off 2 mm of rock surface. Higher rates of erosion (by one to two orders of magnitude) are associated with the degradation of small craters via sand abrasion and infill (Golombek et al., 2014), which would erode rock tails in 2,000 to 20,000 years. Thus, a strong case can be made that the Ca-Cl-rich crusts are being periodically renewed in very recent times.

5. Marquette Island

Marquette Island is ~30×30 cm, wedge-shaped block standing on end on the hematite plains (Figure 18a) roughly 11,800 meters from the Endeavour crater rim. The side of first approach (front side) is dust covered, but the top is relatively dust free. We investigated brushed and abraded targets on the front side and an untreated target on the top. The top surface shows an irregular, granular morphology with lineations roughly parallel to the flat front side (Figure 18b). The MI image of the untreated top surface shows angular-blocky to rounded grains in a fine-grained matrix (Figure 18c). The MI image from the abrasion hole shows clasts of differing brightness, some darker than the matrix, some brighter (Figure 18d). The larger clast-supported grains are poorly sorted, with no preferred orientation; there is no evidence for sedimentary structures or layering. There are instances of what appear to be semi-arcuate structures (Figure 18d), which suggests
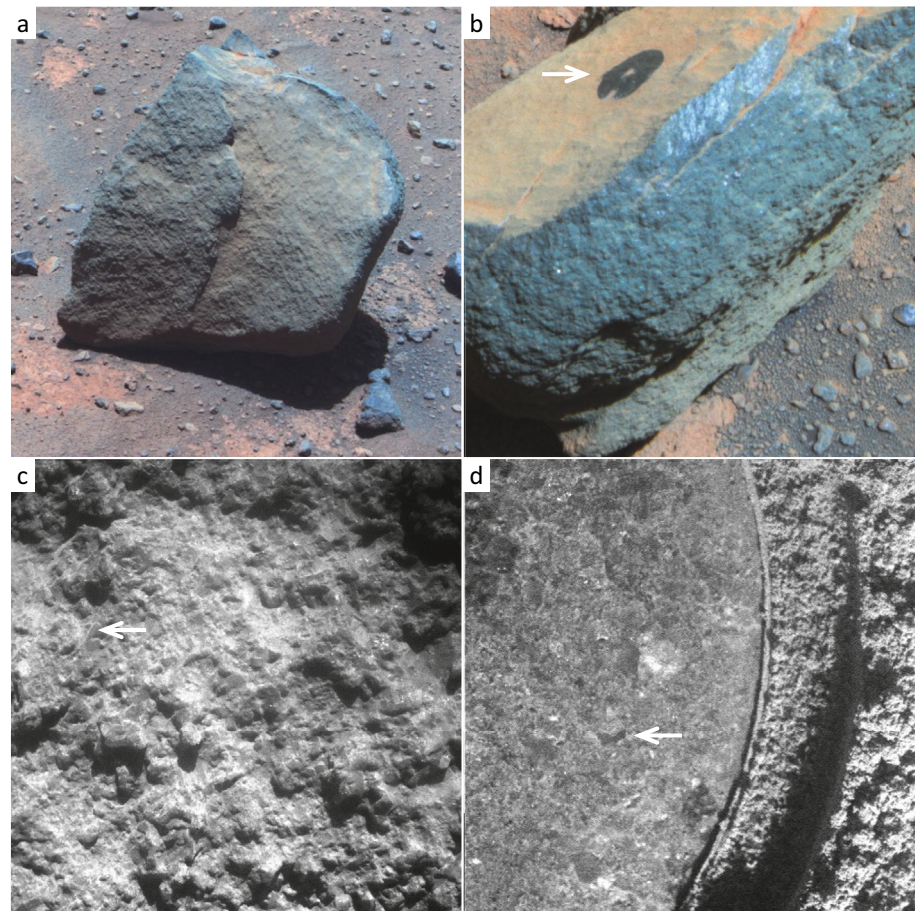
Figure 18. (a) Pancam false-color image (Sol 2063, L257) of the front, dusty side of Marquette Island. The front face is roughly 30×30 cm in size. (b) Pancam false-color image (Sol 2089, L257) of the relatively dust-free top of Marquette Island. Peck Bay brush circle (front face, arrow) is 45 mm in diameter. (c) Microscopic Imager (MI) image of the hackly top surface of Marquette Island. Arrow points out thin, possible alteration vein. Image is 31 mm across. (d) Portion of an MI image of the abrasion hole showing clastic texture. Arrow points out arcuate, possible glass shard. Image is 15.5 mm across.

the rock may contain what might have been glassy shards; the semi-arcuate structures are not common. Bright veins ~100 μm by ~2–3 mm are present (Figure 18c), suggesting localized alteration. The texture is not highly diagnostic of a process or origin but is grossly like the target Seminole on the Columbia Hills in Gusev crater. Yingst et al. (2007) considered Seminole to be part of a tephra sequence, while Crumpler et al. (2011) also included impact ejecta and epiclastic origins as possible modes of formation for clastic rocks on Columbia Hills, including Seminole.

The Mössbauer spectrometer was still active for the investigation of Marquette Island, and two targets were investigated; the APXS compositions were very similar and the Mössbauer data were combined and reduced as a single spectrum. The major iron-bearing minerals are olivine (70% of the Fe), pyroxene (24%) and nanophase ferric oxide (6%). This gives $Fe_{oliv} / (Fe_{oliv} + Fe_{pyx}) = 0.72$, and Fe^{3+}/Σ_{Fe} is 0.06. The nanophase ferric oxide is plausibly contained in dust coatings; there is no indication of Fe-bearing alteration phases. This is consistent with results expected of a very fresh magmatic rock or a breccia composed of such rocks.

Seven APXS measurements were made on Marquette Island, one on an untreated target on the top side, two on brushed spots on the front side, and four analyses in an abrasion hole on the front side; we concentrate here on the abraded targets. Marquette Island is compositionally distinct from all other materials analyzed by Opportunity; all analyses are members of cluster 15 in the first AHCA model with only a single interloper of another rock type (Table 4a; Figure M07), and are the sole residents of cluster 13 when the mobile
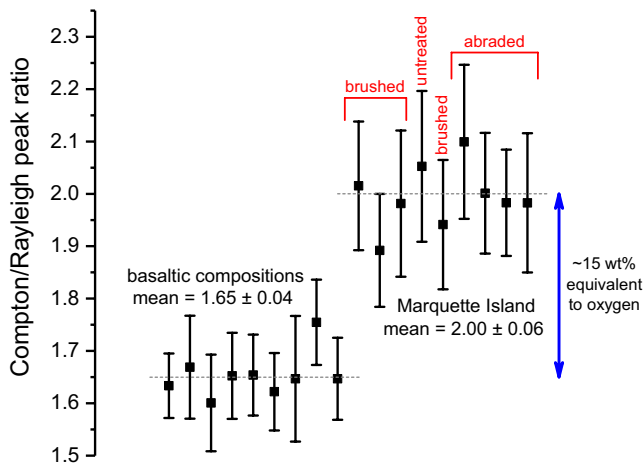
Figure 19. Compton/Rayleigh scatter peak ratio for Marquette Island analyses compared to those of compositionally similar basalts.

elements are excluded (Table 4b; Figure M13). Marquette Island is lower in SiO_2 and TiO_2, and higher in MgO and Cr_2O_3 than Shoemaker formation breccias, the Matijevic formation or average Mars crust (Figure 6). The closest compositional match to Marquette Island among materials studied by the MER mission are Adirondack-class basalts from Gusev crater but Marquette Island has higher MgO and lower CaO than the those.

The APXS spectra of Marquette Island includes scatter peaks that can be used to calculate excesses in light elements ($Z < 11$) in them compared to other samples of broadly similar composition. For geological samples, H, O, and C are the most likely light elements. The scatter peaks arise from elastic (Rayleigh) and inelastic (Compton) scattering of Pu L_α X-rays emitted from the ^{244}Cm source. Rayleigh and Compton scattering cross sections have different Z dependencies for the X-rays. The fitted Compton/Rayleigh intensity ratio can be compared to a theoretically derived ratio based on measured oxide concentrations; if the two are identical, low Z elements are not present at significant quantities (see Campbell et al., 2008). An additional assumption is that the sample is homogeneous. The scatter peaks are sensitive to the overall composition of the sample at greater depth than sampled by the APXS for major elements.

Therefore, a different composition at greater depth could cause differences in Compton/Rayleigh ratios that mimic a composition with excesses in $Z < 11$ elements.

The Compton/Rayleigh scatter peak ratio for individual Marquette Island spectra are compared to several spectra from basaltic rocks and soils that are closest in composition to Marquette Island from Meridiani Planum and Gusev crater (Figure 19). The mean ratio for the Marquette Island spectra is well-resolved from that of the other basaltic composition targets. The Compton/Rayleigh ratios from the four abraded targets are not significantly different from those of the brushed and untreated targets indicating that an artifact of a heterogeneously layered surface can be ruled out. The scatter-peak data indicate an excess of light elements equivalent to ∼15% excess oxygen in Marquette Island compared to other similar martian basaltic compositions.

Of the plausible light elements, additional O alone can be ruled out because the Mössbauer spectra show that the Fe_2O_3 content is negligible and there are no other multivalent major elements that could be at higher oxidation state than normal. Hydrogen (OH^- and/or H_2O) and CO_2 are possible candidates. (We exclude the possibility of abundant organic compounds or elemental C.) The ∼15 wt% equivalent oxygen translates to ∼14 wt% OH^-, ∼13 wt% H_2O or ∼5.5 wt% CO_2. We cannot determine which phase(s) might be present, but any carbonate or H-bearing phase cannot contain Mössbauer-detectable amounts of Fe. Regardless, despite the low ferric iron content that argues for a pristine rock, Marquette Island is either altered, or composed of near-pristine igneous clastic materials cemented by volatile-bearing phases such as magnesite, calcite, kieserite, etc. Marquette Island might be like Peace from Gusev crater: A clastic rock bound by a cementing agent (Squyres, Arvidson, Blaney, et al., 2006). Peace was the weakest rock abraded in Gusev crater based on the specific grind energies calculated from the abrasion activity (1.4 J/mm³ vs. 2.5–44.8 for other rocks, Thomson et al., 2013), and is much lower than the value for Marquette Island (11.5 J/mm³). Peace is posited to be comprised of basaltic grains cemented by Mg- and Ca-sulfates (Ming et al., 2006). The greater strength and low-Z element content of Marquette Island indicates that this rock is plausibly a well-lithified, carbonate-cemented clastic rock of basaltic sand.

We conclude that Marquette Island is an ejecta block lying on the Burns formation indicating that the source crater for it is penecontemporaneous with, or postdates, deposition of the Burns sulfate sandstones. (If the former is correct, then Marquette Island is a lag boulder that was exhumed from the Burns formation.) Two nearby craters penetrate the Burns formation and excavated the underlying Noachian units. Iazu Crater is 6.8 km in diameter and located roughly 25 km south of Endeavour crater; it exposes a section of Burns formation overlying a lower section of altered basaltic composition crust (Powell et al., 2017). Bopolu Crater is 19 km in diameter and situated roughly 65 km southwest of Endeavour crater; it exposes a section

of Meridiani plains rocks above the Noachian basement (Grant et al., 2016). Marquette Island plausibly is a fragment of the Noachian basement from one of these craters.

6. Nature of the Subdued Cratered Unit

The geologic map of Meridiani Planum (Hynek & Di Achille, 2017) shows an expanse of the Noachian subdued cratered unit 35–55 km south of the region explored by Opportunity (Figure 2). They interpret this unit to be composed of volcanic deposits including lava and pyroclastic flows, impact breccias, impact-melt sheets, and erosional deposits formed via fluvio-lacustrine and aeolian processes. The area immediately surrounding Opportunity for several tens to a hundred km or more in every direction is the Hesperian hematite unit (Hynek & Di Achille, 2017), which Opportunity observations show is a hematite-spherule lag deposit plus aeolian ripples that is from a few cm to about a meter thick (Soderblom et al., 2004; Sullivan et al., 2005). The hematite spherules are weathered out of the Burns formation and thus it is probable that this formation immediately underlies the hematite unit everywhere within the map region (Figure 2).

The Noachian/Hesperian Meridiani upper etched unit directly overlies the subdued cratered unit or the Noachian cratered unit along most of its southern, eastern and northern exposures (Figure 2) (Hynek & Di Achille, 2017). This implies that the lower and middle Meridiani etched plains units could be absent at the Opportunity field site. Hynek and Di Achille (2017) concluded that the upper etched unit was formed as aeolian and/or volcanic deposits that were cemented by groundwater activity. The upper most few meters of this unit consist of the Burns formation, which is mostly sulfate-rich sandstones with a small amount of mudstone (Edgar et al., 2012; Grotzinger et al., 2005). The sandstones are mostly aeolian in origin, but some facies indicate localized fluvial reworking and deposition in a lacustrine setting is possible for some (Edgar et al., 2012, 2014; Grotzinger et al., 2005, 2006; Hayes et al., 2011). The fact that the hematite unit is absent over the Meridiani upper etched unit west, north and east of the area explored by Opportunity implies that classic Burns formation containing hematite concretions might not be present in these areas. This could be because the diagenetic processes that form the hematite spherules (McLennan et al., 2005) did not occur in those regions, because the Meridiani upper etched unit there is distinct from the Burns formation, or because the Burns formation and hematite unit have been eroded away.

Supporting evidence that the Burns formation directly overlies the subdued cratered unit in the region explored by Opportunity comes from studies of Bopolu and Iazu Craters just south and southwest of Endeavour crater (Figure 2). Bopolu Crater lies inside ancient Miyamoto crater and is younger than Endeavour crater; it postdates deposition and some erosional stripping of the Meridiani plains units that partially fill Miyamoto crater (Grant et al., 2016). The crater wall exposes a Noachian surface directly overlain by layered sulfates of the Meridiani plains (Grant et al., 2016). The Noachian surface represents the floor of Miyamoto crater at the time the layered sulfates were deposited. Iazu Crater lies closer to Endeavour crater and shows a similar stratigraphy in its walls: layered, hydrated-sulfate- and hematite-bearing rocks—Burns formation—directly overlying basaltic composition rocks (spectral determinations of low- and high-Ca pyroxene) that contain smectite (Powell et al., 2017).

The subdued cratered unit at Endeavour crater is represented by the Matijevic formation and the lower units of the Shoemaker formation. These were target rocks at the Endeavour impact site in the region of the western rim. The Matijevic formation is of uncertain origin because its limited exposure and lack of diagnostic structures or textures did not allow for firm conclusions. This formation is composed of fine-grained clastic rocks that could be an air fall deposit of volcaniclastic or impact origin (Crumpler et al., 2015). In contrast, the lower units of the Shoemaker formation are polymict impact breccias based on textures, and the small clast size and low clast to matrix ratio indicates that they represent distal ejecta from at least two impacts. The pitted rocks and dark basaltic rocks in Perseverance Valley are also part of the pre-Endeavour basement. Because the pitted rocks are within a narrow fracture zone, their mode of formation cannot be determined (Tait et al., 2019). The dark rocks that cap Wdowiak Ridge are likely moderately altered volcanic rocks on an exposed, uplifted block of the pre-impact surface (Mittlefehldt, Gellert, et al., 2018). Thus, ground observations by Opportunity are consistent with mapping from orbit on the types of materials that compose the subdued cratered unit and give a more detailed look at the origin of some components of the unit.

Depending on the timing of the Endeavour impact, the upper Shoemaker may also be part of the subdued cratered unit. Grant et al. (2016) concluded that the Endeavour rim was degraded in part by fluvial processes and this is also indicated by modeling of Endeavour crater degradation (Hughes et al., 2019). Fluvial erosional and depositional processes were important in modifying subdued cratered unit surfaces, but not on the overlying Noachian cratered unit (Hynek & Di Achille, 2017).

The very-fine-grained Grasberg formation is of uncertain stratigraphy. It is an airfall deposit that drapes the lower slopes of the eroded Endeavour rim (Crumpler et al., 2015) and thus likely postdates the period of fluvial erosion that degraded the rim. It almost certainly predates deposition of the Burns formation at Endeavour crater (Crumpler et al., 2015; Mittlefehldt, Gellert, et al., 2018). Crumpler et al. (2015) suggested that the Grasberg formation could be part of a widespread, possibly global, unit, and likened it to the Medusae Fossae Formation. In contrast, McCollom and Hynek (2021) have suggested that the Grasberg and Burns formations share closely related sedimentary sources, or possibly a common sedimentary source. It is unclear how the Grasberg formation might fit into the stratigraphy mapped by Hynek and Di Achille (2017).

7. Conclusions

The Shoemaker formation stratigraphy, particularly well-exposed at Marathon Valley, shows two types polymict impact breccia. Upper units are clast-rich with coarser clasts, while lower units are clast-poor with smaller clasts (Crumpler et al., 2020). Studies of impact breccias at terrestrial craters show that vertical size-sorting is not present in ejecta deposits, but that sorting does occur with radial distance from crater rims, with more distal ejecta having a smaller average clast size, and a higher matrix content (Hörz et al., 1983; Oberbeck, 1975). The Shoemaker formation stratigraphy including clast-rich and clast-poor units is thus inconsistent with deposition as a single ejecta deposit from an impact. We conclude that the lower units are more distal ejecta from at least two earlier impacts, and the upper units are proximal ejecta from Endeavour crater. The lower units, plus the Matijevic formation exposed on Cape York, represent part of the pre-Endeavour geology, which we equate with being subunits of the Noachian subdued cratered unit (Hynek & Di Achille, 2017). The lower Shoemaker units represent at least two depositions of distal impact ejecta and attest to the vibrancy of impact processes in the Noachian. The Matijevic formation, considered correlative with the lower Shoemaker units (Crumpler et al., 2020), could also be distal impact ejecta or it could be a volcaniclastic deposit (Crumpler et al., 2015). The Matijevic formation is compositionally distinct from the Shoemaker formation (Crumpler et al., 2015; Mittlefehldt, Gellert, et al., 2018) and attests to the lithic diversity of the subdued crater unit.

Statistical modeling of compositions sans volatile (S, Cl, and Br) and mobile (P, Mn, Ni, and Zn) elements show that the upper and lower subunits of the Shoemaker formation are for the most part indistinguishable. This indicates that lithic material like the lower Shoemaker formation is the major component of the upper Shoemaker. An exception is the Copper Cliff member on Cape York which contains a significant component of the underlying Matijevic formation; a ballistic erosion-sedimentation process was important in deposition of the Copper Cliff member (Mittlefehldt, Gellert, et al., 2018). Modeling that includes the mobile elements shows that Shoemaker formation rocks from Cape York can be distinguished from those on Cape Tribulation. This suggests general differences in style and/or degree of alteration between the two rim segments (cf., Mittlefehldt, Gellert, et al., 2018).

Unique to the pre-Endeavour rocks is alteration involving enrichments in Si and Al in vein-like structures that crosscut outcrops, and formation of smectite. Boxwork veins cutting the Matijevic formation were formed as mixtures of montmorillonite and silica produced by moderate-temperature alteration of bedrock by circumneutral to mildly alkaline fluids under high water/rock conditions (Clark et al., 2016). Red-zone-group rocks form curvilinear traces cutting lower Shoemaker formation bedrock and are enriched in Si, Al, and sometimes Ge, compared to host bedrock. The Ge and a portion of the silica were precipitated from hydrothermal fluids, indicating alteration under high water/rock. Ferric smectite was observed from orbit in a small region on Cape York and in Marathon Valley. The former is in dark veneers on Matijevic formation outcrops (Arvidson et al., 2014), while the latter is hosted in the lower-1 and lower-2 units of the Shoemaker formation. Association of ferric smectite in the Noachian basement is also indicated by observations of

smectite-bearing basaltic-composition rock in the walls of Iazu Crater (Powell et al., 2017) and the floor of Miyamoto crater (Wiseman et al., 2008).

Post-Endeavour alteration is dominated by sulfate formation. Fracture zones in the crater rim include regions of alteration that produced Mg-sulfates as a dominant phase. This plausibly occurred as heated groundwaters circulated through newly formed fractures and thus was closely associated in time with the impact (e.g., Arvidson et al., 2016), or could have occurred at some much later time, for example during the period of fluvial modification of the crater. Ca-sulfate vein formation also occurred, some pre-Endeavour and some much later. Coarse $CaSO_4$-veins in the Grasberg formation and those in the upper Shoemaker formation near the current ridge crest were formed only after the Endeavour rim had been substantially degraded, and likely after deposition of the Burns formation (Arvidson et al., 2014; Crumpler et al., 2015; Mittlefehldt, Gellert, et al., 2018). However, some Ca-sulfate veins were formed during pre-Endeavour times, as demonstrated by veins crosscutting the Matijevic formation (Arvidson et al., 2014; Crumpler et al., 2015; Mittlefehldt, Gellert, et al., 2018). The Ca-sulfate component of the Gasconade composite vein might also be pre-Endeavour.

Endeavour crater is Noachian in age, and thus, the upper Shoemaker unit might also be part of the subdued cratered unit. The degradation of Endeavour crater rim took place when surface waters were actively modifying surface morphology (Hughes et al., 2019), which is characteristic of the subdued crater unit (Hynek & Di Achille, 2017). However, the differences in alteration styles recorded in the upper Shoemaker versus lower Shoemaker and Matijevic formation indicate that the former was deposited after a substantial time gap.

Comparison of compositions of brushed rock surfaces and abraded interiors show systematic differences in Mg content and coupled differences in Ca and Cl that occur over depths of as little as 1–2 mm. These are interpreted as arising from mobilization of near-surface salts by transient thin films of water followed by precipitation at different depths close to and on the surface. The rock surfaces are undergoing wind erosion as demonstrated by rock tails of mm-scale height formed behind erosion-resistant clasts. Estimates of erosion rates on Meridiani Planum indicate that 2 mm of outcrop surface can be removed within 2 million years; possibly much less than this (Golombek et al., 2006, 2014). Thus, Ca-Cl-salt deposition on surfaces must be renewed on this timescale, indicating that salt mobilization by transient water has occurred very recently, and could be ongoing.

Data Availability Statement

All data used in this article are listed in the references, tables, and supplements. All data tables, details of the Agglomerative Hierarchical Cluster Analysis calculations, and locator images for all rock targets discussed are contained in supplementary files hosted on the Open Data Repository (Mittlefehldt et al., 2021). Data for APXS integrations on all rock and soil targets acquired by Opportunity are available on the NASA Planetary Data System website: https://pds-geosciences.wustl.edu/mer/mer1_mer2-m-apxs-5-oxide-sci-v1/merap_2xxx/data/.

References

Aitchison, J. (1994). Principles of compositional data analysis. In T. W. Anderson, K. T. Fang, & I. Olkin (Eds.), *Multivariate analysis and its applications. Institute of mathematical statistics, lecture notes monograph series 24* (pp. 73–81). https://doi.org/10.1214/lnms/1215463786

Andrews-Hanna, J. C., & Lewis, K. W. (2011). Early Mars hydrology: 2. Hydrological evolution in the Noachian and Hesperian epochs. *Journal of Geophysical Research*, *116*(E2), E02007. https://doi.org/10.1029/2010JE003709

Andrews-Hanna, J. C., Phillips, R. J., & Zuber, M. T. (2007). Meridiani Planum and the global hydrology of Mars. *Nature*, *446*(7132), 163–166. https://doi.org/10.1038/nature05594

Arvidson, R. E., Ashley, J. W., Bell, J. F., Chojnacki, M., Cohen, J., Economou, T. E., et al. (2011). Opportunity Mars Rover mission: Overview and selected results from Purgatory ripple to traverses to Endeavour crater. *Journal of Geophysical Research*, *116*(E7), E00F15. https://doi.org/10.1029/2010JE003746

Arvidson, R. E., Squyres, S. W., Bell, J. F., Catalano, J. G., Clark, B. C., Crumpler, L. S., et al. (2014). Ancient aqueous environments at endeavour crater, Mars. *Science*, *343*(6169), 1248097. https://doi.org/10.1126/science.1248097

Arvidson, R. E., Squyres, S. W., Morris, R. V., Knoll, A. H., Gellert, R., Clark, B. C., et al. (2016). High concentrations of manganese and sulfur in deposits on Murray Ridge, Endeavour crater, Mars. *American Mineralogist*, *101*(6), 1389–1405. https://doi.org/10.2138/am-2016-5599

Baloga, S. M., Fagents, S. A., & Mouginis-Mark, P. J. (2005). Emplacement of Martian rampart crater deposits. *Journal of Geophysical Research*, *110*(E10). https://doi.org/10.1029/2004JE002338

Barlow, N. G. (2005). A review of Martian impact crater ejecta structures and their implications for target properties. In T. Kenkmann, F. Hörz, & A. Deutsch (Eds.), Large meteorite impacts III (Vol. 384, pp. 433–442): Geological Society of America, Special Paper. https://doi.org/10.1130/0-8137-2384-1.433

Barlow, N. G. (2010). What we know about Mars from its impact craters. *Geological Society of America Bulletin*, *122*(5–6), 644–657. https://doi.org/10.1130/b30182.1

Bell, J. F., III, Squyres, S. W., Herkenhoff, K. E., Maki, J. N., Arneson, H. M., Brown, D., et al. (2003). Mars exploration rover Athena panoramic camera (Pancam) investigation. *Journal of Geophysical Research: Planets*, *108*(E12), 108. https://doi.org/10.1029/2003JE002070

Berger, J. A., Schmidt, M. E., Gellert, R., Boyd, N. I., Desouza, E. D., Flemming, R. L., et al. (2017). Zinc and germanium in the sedimentary rocks of Gale crater on Mars indicate hydrothermal enrichment followed by diagenetic fractionation. *Journal of Geophysical Research: Planets*, *122*(8), 1747–1772. https://doi.org/10.1002/2017je005290

Bernstein, L. R. (1985). Germanium geochemistry and mineralogy. *Geochimica et Cosmochimica Acta*, *49*(11), 2409–2422. https://doi.org/10.1016/0016-7037(85)90241-8

Bray, V. J., Tornabene, L. L., Keszthelyi, L. P., McEwen, A. S., Hawke, B. R., Giguere, T. A., et al. (2010). New insight into lunar impact melt mobility from the LRO camera. *Geophysical Research Letters*, *37*(21). https://doi.org/10.1029/2010gl044666

Brown, A. J., Hook, S. J., Baldridge, A. M., Crowley, J. K., Bridges, N. T., Thomson, B. J., et al. (2010). Hydrothermal formation of clay-carbonate alteration assemblages in the Nili Fossae region of Mars. *Earth and Planetary Science Letters*, *297*(1–2), 174–182. https://doi.org/10.1016/j.epsl.2010.06.018

Cabrol, N. A., Herkenhoff, K., Knoll, A. H., Farmer, J., Arvidson, R., Grin, E., et al. (2014). Sands at Gusev crater, Mars. *Journal of Geophysical Research: Planets*, *119*(5), 941–967. https://doi.org/10.1002/2013je004535

Campbell, J. L., Gellert, R., Lee, M., Mallett, C. L., Maxwell, J. A., & O'Meara, J. M. (2008). Quantitative in situ determination of hydration of bright high-sulfate Martian soils. *Journal of Geophysical Research: Planets*, *113*(E6). https://doi.org/10.1029/2007je002959

Carr, M. H., Crumpler, L. S., Cutts, J. A., Greeley, R., Guest, J. E., & Masursky, H. (1977). Martian impact craters and emplacement of ejecta by surface flow. *Journal of Geophysical Research*, *82*(28), 4055–4065. https://doi.org/10.1029/js082i028p04055

Chayes, F. (1971). *Ratio correlation: A manual for students of petrology and geochemistry* (p. 99): University of Chicago Press.

Chen, J., Dai, F., & Yao, X. (2008). Holocene debris-flow deposits and their implications on the climate in the upper Jinsha River valley, China. *Geomorphology*, *93*(3–4), 493–500. https://doi.org/10.1016/j.geomorph.2007.03.011

Clark, B. C., Arvidson, R. E., Gellert, R., Morris, R. V., Ming, D. W., Richter, L., et al. (2007). Evidence for montmorillonite or its compositional equivalent in Columbia Hills, Mars. *Journal of Geophysical Research: Planets*, *112*, E06S01. https://doi.org/10.1029/2006JE002756

Clark, B. C., Morris, R. V., Herkenhoff, K. E., Farrand, W. H., Gellert, R., Jolliff, B. L., et al. (2016). Esperance: Multiple episodes of aqueous alteration involving fracture fills and coatings at Matijevic Hill, Mars. *American Mineralogist*, *101*(7), 1515–1526. https://doi.org/10.2138/am-2016-5575

Crumpler, L. S., Arvidson, R. E., Bell, J., Clark, B. C., Cohen, B. A., Farrand, W. H., et al. (2015). Context of ancient aqueous environments on Mars from in situ geologic mapping at Endeavour crater. *Journal of Geophysical Research: Planets*, *120*(3), 538–569. https://doi.org/10.1002/2014JE004699

Crumpler, L. S., Arvidson, R. E., Mittlefehldt, D. W., Grant, J. A., & Farrand, W. H. (2019). In *Situ mapping of the structural and stratigraphic complexities of Endeavour crater's rim.& the Athena science team. Paper Presented at 50th Lunar and Planetary Science Conference.*

Crumpler, L. S., Arvidson, R. E., Mittlefehldt, D. W., Grant, J. A., & Farrand, W. H. (2020). Results from the first geologic traverse on the topographic rim of a complex impact crater, Endeavour Crater, Mars. *Geology*, *48*(3), 252–257. https://doi.org/10.1130/G46903.1

Crumpler, L. S., Arvidson, R. E., Squyres, S. W., McCoy, T., Yingst, A., Ruff, S., et al. (2011). Field reconnaissance geologic mapping of the Columbia Hills, Mars, based on Mars Exploration Rover Spirit and MRO HiRISE observations. *Journal of Geophysical Research*, *116*(E7). https://doi.org/10.1029/2010je003749

Dressler, B. O., & Reimold, W. U. (2001). Terrestrial impact melt rocks and glasses. *Earth-Science Reviews*, *56*(1–4), 205–284. https://doi.org/10.1016/s0012-8252(01)00064-2

Edgar, L. A., Grotzinger, J. P., Bell, J. F., III, & Hurowitz, J. A. (2014). Hypotheses for the origin of fine-grained sedimentary rocks at Santa Maria crater, Meridiani Planum. *Icarus*, *234*, 36–44. https://doi.org/10.1016/j.icarus.2014.02.019

Edgar, L. A., Grotzinger, J. P., Hayes, A. G., Rubin, D. M., Squyres, S. W., Bell, J. F., & Herkenhoff, K. E. (2012). Stratigraphic architecture of bedrock reference section, Victoria crater, Meridiani Planum, Mars. *Sedimentary Geology of Mars*. *102*. 195–209. SEPM Special Publication. https://doi.org/10.2110/pec.12.102.0195

Eggleton, R. A., Foudoulis, C., & Varkevisser, D. (1987). Weathering of basalt: Changes in rock chemistry and mineralogy. *Clays and Clay Minerals*, *35*(3), 161–169. https://doi.org/10.1346/ccmn.1987.0350301

Ehlmann, B. L., Mustard, J. F., Murchie, S. L., Poulet, F., Bishop, J. L., Brown, A. J., et al. (2008). Orbital identification of carbonate-bearing rocks on Mars. *Science*, *322*(5909), 1828–1832. https://doi.org/10.1126/science.1164759

Escoube, R., Rouxel, O. J., Edwards, K., Glazer, B., & Donard, O. F. (2015). Coupled Ge/Si and Ge isotope ratios as geochemical tracers of seafloor hydrothermal systems: Case studies at Loihi Seamount and East Pacific Rise 9 50′ N. *Geochimica et Cosmochimica Acta*, *167*, 93–112. https://doi.org/10.1016/j.gca.2015.06.025

Farrand, W. H., Johnson, J. R., Bell, J. F., III, & Mittlefehldt, D. W. (2016). *VNIR multispectral observations of rocks at Spirit of St. Louis crater and Marathon Valley on the rim of Endeavour crater made by the opportunity rover Pancam.* Planetary Science Conference.

Farrand, W. H., Johnson, J. R., Bell, J. F., III, Mittlefehldt, D. W., Schröder, C., Tait, A., et al. (2019). Spectral variability among rocks and soils in Perseverance Valley, Mars as observed by the opportunity Pancam. In *Paper Presented at 50th Lunar and Planetary Science Conference.*

Fedo, C. M., McGlynn, I. O., & McSween, H. Y., Jr (2015). Grain size and hydrodynamic sorting controls on the composition of basaltic sediments: Implications for interpreting Martian soils. *Earth and Planetary Science Letters*, *423*, 67–77. https://doi.org/10.1016/j.epsl.2015.03.052

Fox, V. K., Arvidson, R. E., Guinness, E. A., McLennan, S. M., Catalano, J. G., Murchie, S. L., & Powell, K. E. (2016). Smectite deposits in Marathon Valley, Endeavour crater, Mars, identified using CRISM hyperspectral reflectance data. *Geophysical Research Letters*, *43*, 4885–4892. https://doi.org/10.1002/2016GL069108

Gellert, R., Rieder, R., Brückner, J., Clark, B. C., Dreibus, G., Klingelhöfer, G., et al. (2006). Alpha Particle X-Ray Spectrometer (APXS): Results from Gusev crater and calibration report. *Journal of Geophysical Research*, *111*(E2), E02S05. https://doi.org/10.1029/2005JE002555

Golombek, M. P., Grant, J. A., Crumpler, L. S., Greeley, R., Arvidson, R. E., Bell, J. F., III, et al. (2006). Erosion rates at the Mars Exploration Rover landing sites and long-term climate change on Mars. *Journal of Geophysical Research*. *111*(E12). https://doi.org/10.1029/2006JE002754

Golombek, M. P., Warner, N. H., Ganti, V., Lamb, M. P., Parker, T. J., Fergason, R. L., & Sullivan, R. (2014). Small crater modification on Meridiani Planum and implications for erosion rates and climate change on Mars. *Journal of Geophysical Research: Planets*, *119*(12), 2522–2547. https://doi.org/10.1002/2014JE004658

Gorevan, S. P., Myrick, T., Davis, K., Chau, J. J., Bartlett, P., Mukherjee, S., et al. (2003). Rock abrasion tool: Mars exploration rover mission. *Journal of Geophysical Research*. *108*(E12). https://doi.org/10.1029/2003je002061

Grant, J. A., Crumpler, L. S., Parker, T. J., Golombek, M. P., Wilson, S. A., & Mittlefehldt, D. W. (2015). *Degradation of endeavour crater, Mars. Planetary science conference*.

Grant, J. A., Parker, T. J., Crumpler, L. S., Wilson, S. A., Golombek, M. P., & Mittlefehldt, D. W. (2016). The degradational history of Endeavour crater, Mars. *Icarus*, *280*, 22–36. https://doi.org/10.1016/j.icarus.2015.08.019

Grieve, R. A., & Therriault, A. M. (2004). Observations at terrestrial impact structures: Their utility in constraining crater formation. *Meteoritics & Planetary Sciences*, *39*(2), 199–216. https://doi.org/10.1111/j.1945-5100.2004.tb00336.x

Grotzinger, J., Bell, J., III, Herkenhoff, K., Johnson, J., Knoll, A., McCartney, E., et al. (2006). Sedimentary textures formed by aqueous processes, Erebus crater, Meridiani Planum, Mars. *Geology*, *34*(12), 1085–1088. https://doi.org/10.1130/g22985a.1

Grotzinger, J. P., Arvidson, R. E., Bell, J. F., III, Calvin, W., Clark, B. C., Fike, D. A., et al. (2005). Stratigraphy and sedimentology of a dry to wet eolian depositional system, Burns formation, Meridiani Planum, Mars. *Earth and Planetary Science Letters*, *240*(1), 11–72. https://doi.org/10.1016/j.epsl.2005.09.039

Hayes, A. G., Grotzinger, J. P., Edgar, L. A., Squyres, S. W., Watters, W. A., & Sohl-Dickstein, J. (2011). Reconstruction of eolian bed forms and paleocurrents from cross-bedded strata at Victoria Crater, Meridiani Planum, Mars. *Journal of Geophysical Research*, *116*(E7). https://doi.org/10.1029/2010je003688

He, D., Lee, C. T. A., Yu, X., & Farner, M. (2019). Ge/Si partitioning in igneous systems: Constraints from laser ablation ICP-MS measurements on natural samples. *Geochemistry, Geophysics, Geosystems*, *20*(10), 4472–4486. https://doi.org/10.1029/2019gc008514

Herkenhoff, K. E., Squyres, S. W., Bell, J. F., Maki, J. N., Arneson, H. M., Bertelsen, P., et al. (2003). Athena Microscopic Imager investigation. *Journal of Geophysical Research*. *108*(E12). https://doi.org/10.1029/2003je002076

Hörz, F., Ostertag, R., & Rainey, D. A. (1983). Bunte Breccia of the Ries: Continuous deposits of large impact craters. *Reviews of Geophysics*, *21*(8), 1667–1725. https://doi.org/10.1029/RG021i008p01667

Hughes, M. N., Arvidson, R. E., Grant, J. A., Wilson, S. A., Howard, A. D., & Golombek, M. P. (2019). Degradation of Endeavour crater based on orbital and rover-based observations in combination with landscape evolution modeling. *Journal of Geophysical Research: Planets*, *124*(6), 1472–1494. https://doi.org/10.1029/2019je005949

Hurowitz, J. A., & McLennan, S. M. (2007). A∼ 3.5 Ga record of water-limited, acidic weathering conditions on Mars. *Earth and Planetary Science Letters*, *260*(3–4), 432–443. https://doi.org/10.1016/j.epsl.2007.05.043

Hynek, B. M., Arvidson, R. E., & Phillips, R. J. (2002). Geologic setting and origin of Terra Meridiani hematite deposit on Mars. *Journal of Geophysical Research: Planets*, *107*(E10), 5088. https://doi.org/10.1029/2002je001891

Hynek, B. M., & Di Achille, G. (2017). Geologic map of Meridiani Planum, Mars. (Vol. 3356): Scientific Investigations MapU.S. Geological Survey. https://doi.org/10.3133/sim3356

Hynek, B. M., & Phillips, R. J. (2008). The stratigraphy of Meridiani Planum, Mars, and implications for the layered deposits' origin. *Earth and Planetary Science Letters*, *274*(1–2), 214–220. https://doi.org/10.1016/j.epsl.2008.07.025

Johnson, J. R., Bell, J. F., III, Cloutis, E., Staid, M., Farrand, W. H., McCoy, T., et al. (2007). Mineralogic constraints on sulfur-rich soils from Pancam spectra at Gusev crater, Mars. *Geophysical Research Letters*, *34*(13), L13202. https://doi.org/10.1029/2007GL029894

Jolliff, B. L., Mittlefehldt, D. W., Farrand, W. H., Knoll, A. H., McLennan, S. M., & Gellert, R. (2019). Mars exploration rover opportunity: Water and other volatiles on ancient Mars. In J. Filiberto, & S. P. Schwenzer (Eds.), *Volatiles in the martian crust* (pp. 285–328): Elsevier. https://doi.org/10.1016/B978-0-12-804191-8.00010-6

Klingelhöfer, G., Morris, R. V., Bernhardt, B., Rodionov, D., de Souza, P. A., Jr, Squyres, S. W., et al. (2003). Athena MIMOS II Mössbauer spectrometer investigation. *Journal of Geophysical Research*, *108*(E12), 108. https://doi.org/10.1029/2003JE002138

Macdonald, R., McGarvie, D. W., Pinkerton, H., Smith, R. L., & Palacz, A. (1990). Petrogenetic evolution of the Torfajökull Volcanic Complex, Iceland I. Relationship between the magma types. *Journal of Petrology*, *31*(2), 429–459. https://doi.org/10.1093/petrology/31.2.429

Mader, M. M., & Osinski, G. R. (2018). Impactites of the Mistastin Lake impact structure: Insights into impact ejecta emplacement. *Meteoritics & Planetary Sciences*, *53*(12), 2492–2518. https://doi.org/10.1111/maps.13173

Maloof, A. C., Stewart, S. T., Weiss, B. P., Soule, S. A., Swanson-Hysell, N. L., Louzada, K. L., et al. (2010). Geology of lonar crater, India. *Geological Society of America Bulletin*. *122*, pp. 109–126. https://doi.org/10.1130/b26474.1

Masaitis, V. L. (1999). Impact structures of northeastern Eurasia: The territories of Russia and adjacent countries. *Meteoritics & Planetary Sciences*, *34*(5), 691–711. https://doi.org/10.1111/j.1945-5100.1999.tb01381.x

McCollom, T. M., & Hynek, B. (2021). Geochemical data indicate highly similar sediment compositions for the Grasberg and Burns formations on Meridiani Planum, Mars. *Earth and Planetary Science Letters*, *557*, 116729. https://doi.org/10.1016/j.epsl.2020.116729

McGlynn, I. O., Fedo, C. M., & McSween, H. Y., Jr (2012). Soil mineralogy at the Mars Exploration Rover landing sites: An assessment of the competing roles of physical sorting and chemical weathering. *Journal of Geophysical Research*, *117*(E1). https://doi.org/10.1029/2011je003861

McLennan, S. M., Bell, J. F., III, Calvin, W. M., Christensen, P. R., Clark, B. D., De Souza, P. A., et al. (2005). Provenance and diagenesis of the evaporite-bearing Burns formation, Meridiani Planum, Mars. *Earth and Planetary Science Letters*, *240*(1), 95–121. https://doi.org/10.1016/j.epsl.2005.09.041

McSween, H. Y., Wyatt, M. B., Gellert, R., Bell, J. F., Morris, R. V., Herkenhoff, K. E., et al. (2006). Characterization and petrologic interpretation of olivine-rich basalts at Gusev Crater, Mars. *Journal of Geophysical Research: Planets*, *111*(E2). https://doi.org/10.1029/2006je002698

Melosh, H. J. (1989). *Impact cratering: A geologic process* (p. 253)New York: Oxford University Press.

Meunier, A., Caner, L., Hubert, F., El Albani, A., & Prêt, D. (2013). The weathering intensity scale (WIS): An alternative approach of the chemical index of alteration (CIA). *American Journal of Science*, *313*(2), 113–143. https://doi.org/10.2475/02.2013.03

Ming, D. W., Mittlefehldt, D. W., Morris, R. V., Golden, D. C., Gellert, R., Yen, A., et al. (2006). Geochemical and mineralogical indicators for aqueous processes in the Columbia Hills of Gusev Crater, Mars. *Journal of Geophysical Research: Planets*, *111*, E02S12. https://doi.org/10.1029/2005JE002560

Mittlefehldt, D. W., Arvidson, R. E., Crumpler, L. S., Farrand, W. H., Gellert, R., Grant, J. A., et al. (2019). *Geochemistry of Noachian bedrock and alteration events, Endeavour crater, Mars. Paper presented at 50th lunar and planetary science conference*.

Mittlefehldt, D. W., Crumpler, L. S., Grant, J. A., Arvidson, R. E., & Farrand, W. H. (2018). *Noachian-aged pre-impact lithology exposed in Endeavour crater rim: Mars Exploration Rover Opportunity observations*. Paper presented at 2018. Geological Society of America Annual Meeting.

Mittlefehldt, D. W., Gellert, R., Herkenhoff, K. E., Morris, R. V., Clark, B. C., Cohen, B. A., et al. (2010). Marquette Island: A distinct mafic lithology discovered by opportunity. In *Paper Presented at 41st Lunar and Planetary Science Conference*.

Mittlefehldt, D. W., Gellert, R., Ming, D. W., & Yen, A. S. (2019). Alteration processes in Gusev crater, Mars: Volatile/mobile element contents of rocks and soils determined by the Spirit Rover. In J. Filiberto, & S. P. Schwenzer (Eds.), *Volatiles in the martian crust* (pp. 329–368): Elsevier. https://doi.org/10.1016/B978-0-12-804191-8.00011-8

Mittlefehldt, D. W., Gellert, R., Ming, D. W., Yen, A. S., Clark, B. C., Morris, R. V., et al. (2018). Diverse lithologies and alteration events on the rim of Noachian-aged Endeavour crater, Meridiani Planum, Mars: In situ compositional evidence. *Journal of Geophysical Research: Planets*, *123*(5), 1255–1306. https://doi.org/10.1002/2017JE005474

Mittlefehldt, D. W., Gellert, R., vanBommel, S., Arvidson, R. E., Ashley, J. W., Clark, B. C., et al. (2021). *Noachian bedrock at Endeavour crater: Data tables, statistical modeling and locator images. Open data repository*. https://doi.org/10.48484/nj11-8k34

Morris, R. V., Ruff, S. W., Gellert, R., Ming, D. W., Arvidson, R. E., Clark, B. C., et al. (2010). Identification of carbonate-rich outcrops on Mars by the Spirit rover. *Science*, *329*(5990), 421–424. https://doi.org/10.1126/science.1189667

Mortlock, R. A., Froelich, P. N., Feely, R. A., Massoth, G. J., Butterfield, D. A., & Lupton, J. E. (1993). Silica and germanium in Pacific Ocean hydrothermal vents and plumes. *Earth and Planetary Science Letters*, *119*(3), 365–378. https://doi.org/10.1016/0012-821x(93)90144-x

Nesbitt, H. W., & Wilson, R. E. (1992). Recent chemical weathering of basalts. *American Journal of Science*, *292*(10), 740–777. https://doi.org/10.2475/ajs.292.10.740

Newsom, H. E., Barber, C. A., Hare, T. M., Schelble, R. T., Sutherland, V. A., & Feldman, W. C. (2003). Paleolakes and impact basins in southern Arabia Terra, including Meridiani Planum: Implications for the formation of hematite deposits on Mars. *Journal of Geophysical Research*, *108*(E12). https://doi.org/10.1029/2002JE001993

Newsom, H. E., Lanza, N. L., Ollila, A. M., Wiseman, S. M., Roush, T. L., Marzo, G. A., et al. (2010). Inverted channel deposits on the floor of Miyamoto crater, Mars. *Icarus*, *205*(1), 64–72. https://doi.org/10.1016/j.icarus.2009.03.030

Niles, P. B., Catling, D. C., Berger, G., Chassefière, E., Ehlmann, B. L., Michalski, J. R., et al. (2013). Geochemistry of carbonates on Mars: Implications for climate history and nature of aqueous environments. *Space Science Reviews*, *174*(1), 301–328. https://doi.org/10.1007/s11214-012-9940-y

Oberbeck, V. R. (1975). The role of ballistic erosion and sedimentation in lunar stratigraphy. *Reviews of Geophysics*, *13*(2), 337–362. https://doi.org/10.1029/RG013i002p00337

Osinski, G. R., Tornabene, L. L., & Grieve, R. A. (2011). Impact ejecta emplacement on terrestrial planets. *Earth and Planetary Science Letters*, *310*(3–4), 167–181. https://doi.org/10.1016/j.epsl.2011.08.012

Parker, T. J., Golombek, M. P., Calef, F. J., & Hare, T. M. (2012). *High-resolution basemaps for localization, mission planning, and geologic mapping at Meridiani Planum and Gale crater. Paper presented at 43rd lunar and planetary science conference*.

Pokrovski, G. S., & Schott, J. (1998). Thermodynamic properties of aqueous Ge (IV) hydroxide complexes from 25 to 350 C: Implications for the behavior of germanium and the Ge/Si ratio in hydrothermal fluids. *Geochimica et Cosmochimica Acta*, *62*(9), 1631–1642. https://doi.org/10.1016/s0016-7037(98)00081-7

Powell, K. E., Arvidson, R. E., Zanetti, M., Guinness, E. A., & Murchie, S. L. (2017). The structural, stratigraphic, and paleoenvironmental record exposed on the rim and walls of Iazu Crater, Mars. *Journal of Geophysical Research: Planets*, *122*(5), 1138–1156. https://doi.org/10.1002/2016je005196

Reimold, W. U. (1995). Pseudotachylite in impact structures—Generation by friction melting and shock brecciation? A review and discussion. *Earth-Science Reviews*, *39*(3–4), 247–265. https://doi.org/10.1016/0012-8252(95)00033-x

Rieder, R., Gellert, R., Brückner, J., Klingelhöfer, G., Dreibus, G., Yen, A., & Squyres, S. W. (2003). The new Athena alpha particle X-ray spectrometer for the Mars Exploration Rovers. *Journal of Geophysical Research*. *108*(E12).

Sautter, V., Toplis, M. J., Wiens, R. C., Cousin, A., Fabre, C., Gasnault, O., et al. (2015). In situ evidence for continental crust on early Mars. *Nature Geoscience*, *8*(8), 605–609. https://doi.org/10.1038/ngeo2474

Schultz, P. H., & Gault, D. E. (1979). Atmospheric effects on Martian ejecta emplacement. *Journal of Geophysical Research*, *84*(B13), 7669–7687. https://doi.org/10.1029/jb084ib13p07669

Shoemaker, E. M. (1963). Impact mechanics at Meteor Crater, Arizona. In B. M. Middlehurst, & G. P. Kuiper (Eds.), *The Moon, meteorites and comets* (pp. 301–336): University of Chicago Press.

Siegert, S., Branney, M. J., & Hecht, L. (2017). Density current origin of a melt-bearing impact ejecta blanket (Ries suevite, Germany). *Geology*, *45*(9), 855–858. https://doi.org/10.1130/g39198.1

Soderblom, L. A., Anderson, R. C., Arvidson, R. E., Bell, J. F., Cabrol, N. A., Calvin, W., et al. (2004). Soils of Eagle crater and Meridiani Planum at the Opportunity rover landing site. *Science*, *306*(5702), 1723–1726. https://doi.org/10.1126/science.1105127

Squyres, S. W., Arvidson, R. E., Baumgartner, E. T., Bell, J. F., Christensen, P. R., Gorevan, S., et al. (2003). Athena Mars rover science investigation. *Journal of Geophysical Research*. *108*(E12). https://doi.org/10.1029/2003je002121

Squyres, S. W., Arvidson, R. E., Bell, J. F., Calef, F., Clark, B. C., Cohen, B. A., et al. (2012). Ancient impact and aqueous processes at Endeavour crater, Mars. *Science*, *336*(6081), 570–576. https://doi.org/10.1126/science.1220476

Squyres, S. W., Arvidson, R. E., Blaney, D. L., Clark, B. C., Crumpler, L., Farrand, W. H., et al. (2006). Rocks of the Columbia hills. *Journal of Geophysical Research*, *111*(E2). https://doi.org/10.1029/2005je002562

Squyres, S. W., Arvidson, R. E., Bollen, D., Bell, J. F., III, Brueckner, J., Cabrol, N. A., et al. (2006). Overview of the opportunity mars exploration rover mission to Meridiani Planum: Eagle crater to purgatory ripple. *Journal of Geophysical Research*, *111*(E12), E12S12. https://doi.org/10.1029/2006je002771

Squyres, S. W., & Knoll, A. H. (2005). Sedimentary rocks at Meridiani Planum: Origin, diagenesis, and implications for life on Mars. *Earth and Planetary Science Letters*, *240*(1), 1–10. https://doi.org/10.1016/j.epsl.2005.09.038

Stöffler, D., Artemieva, N. A., Wünnemann, K., Reimold, W. U., Jacob, J., Hansen, B. K., & Summerson, I. A. (2013). Ries crater and suevite revisited—Observations and modeling Part I: Observations. *Meteoritics & Planetary Sciences*, *48*(4), 515–589. https://doi.org/10.1111/maps.12086

Stopar, J. D., Hawke, B. R., Robinson, M. S., Denevi, B. W., Giguere, T. A., & Koeber, S. D. (2014). Occurrence and mechanisms of impact melt emplacement at small lunar craters. *Icarus*, *243*, 337–357. https://doi.org/10.1016/j.icarus.2014.08.011

Sullivan, R., Banfield, D., Bell, J. F., Calvin, W., Fike, D., Golombek, M., et al. (2005). Aeolian processes at the Mars Exploration Rover Meridiani Planum landing site. *Nature*, *436*(7047), 58–61. https://doi.org/10.1038/nature03641

Tait, A. W., Schröder, C., Farrand, W. H., Ashley, J. W., Cohen, B. A., Gellert, R., et al. (2019). *Exploring origins of pitted/vesicular rocks in Perseverance Valley, Endeavour crater. Paper presented at 50th lunar and planetary science conference*.

Taylor, S. R., & McLennan, S. M. (2009). *Planetary crusts: Their composition, origin and evolution*: Cambridge University Press.

Thomson, B. J., Bridges, N. T., Cohen, J., Hurowitz, J. A., Lennon, A., Paulsen, G., & Zacny, K. (2013). Estimating rock compressive strength from Rock Abrasion Tool (RAT) grinds. *Journal of Geophysical Research: Planets*, *118*(6), 1233–1244. https://doi.org/10.1002/jgre.20061

Viviano, C. E., Moersch, J. E., & McSween, H. Y. (2013). Implications for early hydrothermal environments on Mars through the spectral evidence for carbonation and chloritization reactions in the Nili Fossae region. *Journal of Geophysical Research: Planets*, *118*(9), 1858–1872. https://doi.org/10.1002/jgre.20141

Weiss, D. K., & Head, J. W. (2017). Evidence for stabilization of the ice-cemented cryosphere in earlier Martian history: Implications for the current abundance of groundwater at depth on Mars. *Icarus*. *288*, 120–147. https://doi.org/10.1016/j.icarus.2017.01.018

Wiseman, S. M., Arvidson, R. E., Andrews-Hanna, J. C., Clark, R. N., Lanza, N. L., Des Marais, D., et al. (2008). Phyllosilicate and sulfate-hematite deposits within Miyamoto crater in southern Sinus Meridiani, Mars. *Geophysical Research Letters*. *35*(19), L19204. https://doi.org/10.1029/2008GL035363

Wolters, F., Lagaly, G., Kahr, G., Nueeshch, R., & Emmerich, K. (2009). A comprehensive characterization of dioctahedral smectites. *Clays and Clay Minerals*, *57*(1), 115–133. https://doi.org/10.1346/ccmn.2009.0570111

Wray, J. J., Noe Dobrea, E. Z., Arvidson, R. E., Wiseman, S. M., Squyres, S. W., McEwen, A. S., et al. (2009). Phyllosilicates and sulfates at Endeavour crater, Meridiani Planum, Mars. *Geophysical Research Letters*, *36*(21), L21201. https://doi.org/10.1029/2009gl040734

Yingst, R. A., Schmidt, M. E., Herkenhoff, K. E., Mittlefehldt, D. W., & the Athena Science Team (2007). *Linking home plate and algonquin class rocks through microtextural analysis: Evidence for hydro volcanism in the inner basin of Columbia Hills, Gusev crater. Paper presented at 7th International Conference on Mars.*